FORTÉ observations of lightning radio-frequency signatures: Capabilities and basic results

Abram R. Jacobson[1], Stephen O. Knox, Robert Franz, and Donald C. Enemark

Los Alamos National Laboratory

Abstract

The FORTÉ satellite, launched 29 August 1997, carries both radio-frequency-receiver and optical (imaging and photometric) payloads for the study of lightning. The radio-frequency data for the first seven months of operation are described, both to illustrate the satellite's capabilities, and to explain the basic statistical findings so far. FORTÉ's multi-channel rf trigger system represents a significant advance in space-based monitoring of lightning emissions. We are able to observe even rather weak and diffuse rf emissions from lightning, and are no longer limited to the brightest known events, "trans-ionospheric pulse pairs", or TIPPs. We do see TIPPs, and we show that the FORTÉ observations of TIPPs are consistent only with the second pulse's being due to a ground reflection. We find that TIPPs are basically bimodal in character, one type having a steep roll-off of power from 38 MHz to 130 MHz, and the other being essentially flat-spectrum in that range. The steep-spectrum TIPPs cluster-together in the manner of most rf emissions from lightning, while the flat-spectrum events tend to maintain a wider spacing (>0.1 s) between recurrent emissions.

1. Introduction

Lightning emissions range from ultra-low-frequency (ULF) through ultra-high-frequency (UHF), and also include the visible-light spectrum. This paper describes Very High Frequency (VHF) observations of lightning using a suite of receivers [*Enemark and Shipley*, 1994] aboard the FORTÉ (Fast On-board Recording of Transient Events) satellite launched 29 August 1997. FORTÉ is a joint project of

Sandia National Laboratory and Los Alamos National Laboratory, under the auspices of the United States Department of Energy.

Lightning radio-frequency emissions in the VHF band (30 - 300 MHz) have previously been observed from the Blackbeard payload aboard the Alexis satellite [*Holden et al.*, 1995; *Massey and Holden*, 1995]. The Blackbeard receiver was broadband (75-MHz Nyquist bandwidth; narrower analog bandwidth) and employed a trigger based on instantaneous signal power from the entire analog bandwidth. As a result Blackbeard was somewhat susceptible to TV and FM carrier interference and had difficulty reliably triggering on any but the most intense lightning signatures over inhabited (i.e., radio-noisy) parts of the Earth, due to competition from the man-made noise background. However, Blackbeard reported a unique class of very intense VHF signatures known as "transionospheric pulse pairs", or TIPPs. The name was due to the occurence of two separated pulses, each a few microseconds long, separated by tens of microseconds. These emissions' instantaneous power was at least tenfold greater than that of VHF signatures ordinarily accompanying lightning. Later in the Alexis mission, TIPPs could be observed by Blackbeard even over the continental United States, at least in "high band" (above FM carriers) [*Massey et al.*, 1998]. All authors on TIPPs found clear association with lightning activity [*Holden et al.*, 1995; *Massey and Holden*, 1995; *Zuelsdorf et al.*, 1997].

2. The FORTÉ satellite and rf payload

We provide here only a sketch of FORTÉ's rf capabilities. A longer discussion will be given in a separate engineering paper.

FORTÉ was launched on 29 August 1997 into a 70° inclination orbit, nearly circular at 800 km altitude. Data acquisition commenced within days and has continued without serious interruption through the writing of this paper (April 1998). The FORTÉ satellite

contains both a suite of rf receivers and the Optical Lightning System (comprising a CCD imager and a fast broadband photometer). This paper will introduce the performance and capabilities of the rf payload [*Enemark and Shipley*, 1994] as reflected in rf data gathered during the first seven months of the FORTÉ mission. Follow-on papers will introduce the capabilities and performance of the optical payload and the numerous scientific findings of each payload individually, in concert each other, and coordinated with supporting ground-level measurements of lightning. Additional follow-on papers will describe the engineering design of the satellite and its payloads.

The data reported below are from the narrower-band of the two rf receivers carried by FORTÉ. This narrower-band system contains two independently-tunable passbands, tunable anywhere in the range 20 - 300 MHz. Each passband's signal is analog-filtered to a 22-MHz effective bandwidth and then digitized at 50 Megasamples/s. The greatest advance of FORTÉ over Alexis/Blackbeard is its triggering scheme for these narrow-band receivers: Each receiver's passband has embedded within it eight independent triggering subbands spaced at 2.5-MHz separations, with each subband having 1 MHz of bandwidth. The two 22-MHz receivers are triggered together, so that both are digitized synchronously. The common trigger of the two 22-MHz-wide channels can be either (1) from the internal timer or (2) from a logical OR of a requisite number of subband trigger channels. In the work described here, the trigger derives from coincidence of typically five (out of eight possible) subband triggers.The comb of eight trigger subbands are from one or the other of the two 22-MHz-wide channels, depending on the program. The present study does not used timed data, as we are here interested only in bursts of lightning VHF signal recorded in signal-triggered mode.

Each 1-MHz trigger subband (eight in each 22-MHz-wide channel; sixteen total) has a noise-compensation option, so that the trigger threshhold is either set in absolute level or as db *above a low-pass-filtered noise level* in that 1-MHz subband, i.e. as a "noise-riding threshhold". In this way the trigger system can in practice trigger on lightning signatures that would previously (in Blackbeard) have been overwhelmed by man-made carriers appearing in the overall analog passband. To do this, we locate the selected 1-MHz trigger subbands away from common carriers. In the data used here, we use noise-riding-threshhold triggering and require five (out of eight) 1-MHz subbands to trigger in coincidence (with a coincidence window adequate to compensate for ionospheric dispersion). If any one trigger subband is still noisy due to a carrier, we can toggle it off. We typically require the signal to rise 14 - 20 db (depending on the program and the intended class of lightning signals) above the noise background in each 1-MHz subband contributor to the "5-out-of-8" OR. Although there is the possibility of requiring coincidence from a number of triggers deriving from all sixteen 1-MHz subbands (eight in each 22-MHz channel), we have not commonly used that option, and instead we derive the noise-riding-threshhold 5-out-of-8 OR trigger from one or the other of the 22-MHz channels.

In the data to follow, we typically run with one 22-MHz channel placed in the range 26-48 MHz, with a nominal 38-MHz center ("lo band"), and the other in the range 118 - 140 MHz,with a nominal 130-MHz center ("hi-band"). This allows the VHF signal spectrum to be roughly inferred from the relative power on the two channels. We usually run with lo-band trigger but have done some work with hi-band trigger (see Section 5e below). The reason we prefer lo-band triggering is that this tends to trigger off the more intense part of the signal spectrum.

In the data reported below, each 22-MHz channel since 28 October 1997 is connected to a different linear polarization of a two-polarization log-periodic antenna. The

antenna is mounted on a boom facing the satellite nadir, usually within a few degrees. The antenna is designed to place an approximate null (througout the VHF spectrum) on the limb of the Earth as seen from FORTÉ, and a maximum lobe at nadir. (From 800 km altitude, the limb is located on a "small circle" of arc-diameter 6,400 km.)

During the two months prior to deployment of the log-peridic boom antenna, we used short-monopole active antennas close to the satellite body. Those two months of preliminary data were much noisier than after 28 October 1997, due to the pre-amps into which the active antennas were fed.

The Data Acquisition System (DAS) contains enough memory for up to 0.8 seconds (cumulative) of 12-bit data from each of the 22-MHz channels. Each record is triggered (see above) and has adjustable pre/post-trigger ratio. We typically use 400-μs records with 100 μs of pretrigger samples and 300 μs of posttrigger samples. There is typically room in DAS memory for ~2000 such events between downloads. Since we can have up to several downloads per day, in principle we can acquire up to ~10000 such events per day. Usually, however, operations constraints limit us to less than this theoretical maximum.

The DAS is capable of retriggering a new record within microseconds of the end of the previous record, so that FORTÉ records can effectively mosaic-together to form a quasi-continuous registation of VHF signatures arriving one-upon-the-other within a flash.

3. Sorting of lightning data

The copious data acquisition by FORTÉ has necessitated automation of signal handling and sorting. All rf data taken in lightning surveys by FORTÉ are subjected to a standard automated analysis and databasing as follows:

Each signal-triggered lo-band and hi-band record is subjected to a spectrogram. The spectrogram's Fourier moving time window is 128 samples (=2.56 μs) and is advanced in steps of only 8 samples (=0.16 μs). The spectral resolution is 0.39 MHz. Each spectrogram is then "prewhitened", that is, treated to remove CW carriers (at least in a very crude way). The rows are scored in time-average power (integrating over the whole record), and the top-scoring 50% of the rows (in terms of integrated power) are then multiplied by a factor given by the ratio of their power divided into the median-scoring row of all the rows. Another way of looking at this is that all 50% of rows with the most power are re-scaled so their average power clamps at the median-power row's power.

Figure 1 (left column) shows the prewhitened spectrograms of four typical lo-band lightning signatures. The pixel color codes the logarithm of the power in that time/frequency pixel. The red-through-green dynamic range is ~35 dB. All four panels are alike in having 400-μs record lengths and in being lo-band. Each of the four panels in the left column of Figure 1 shows the distinctive f^{-2} ionospheric dispersion ("chirp"), *approximately* described by a group delay versus frequency f as follows:

$$(\mu s) = 1.34 \times \{N/(10^{17}m^{-2})\} \times \{f/(100MHz)\}^{-2} \qquad (1)$$

where f is the radio frequency, and N is the line-of-sight-integrated total electron content (slant TEC). We next fit N, by optimally aligning the spectrogram into vertical features (occuring throughout the band simultaneously). The right column of Figure 1
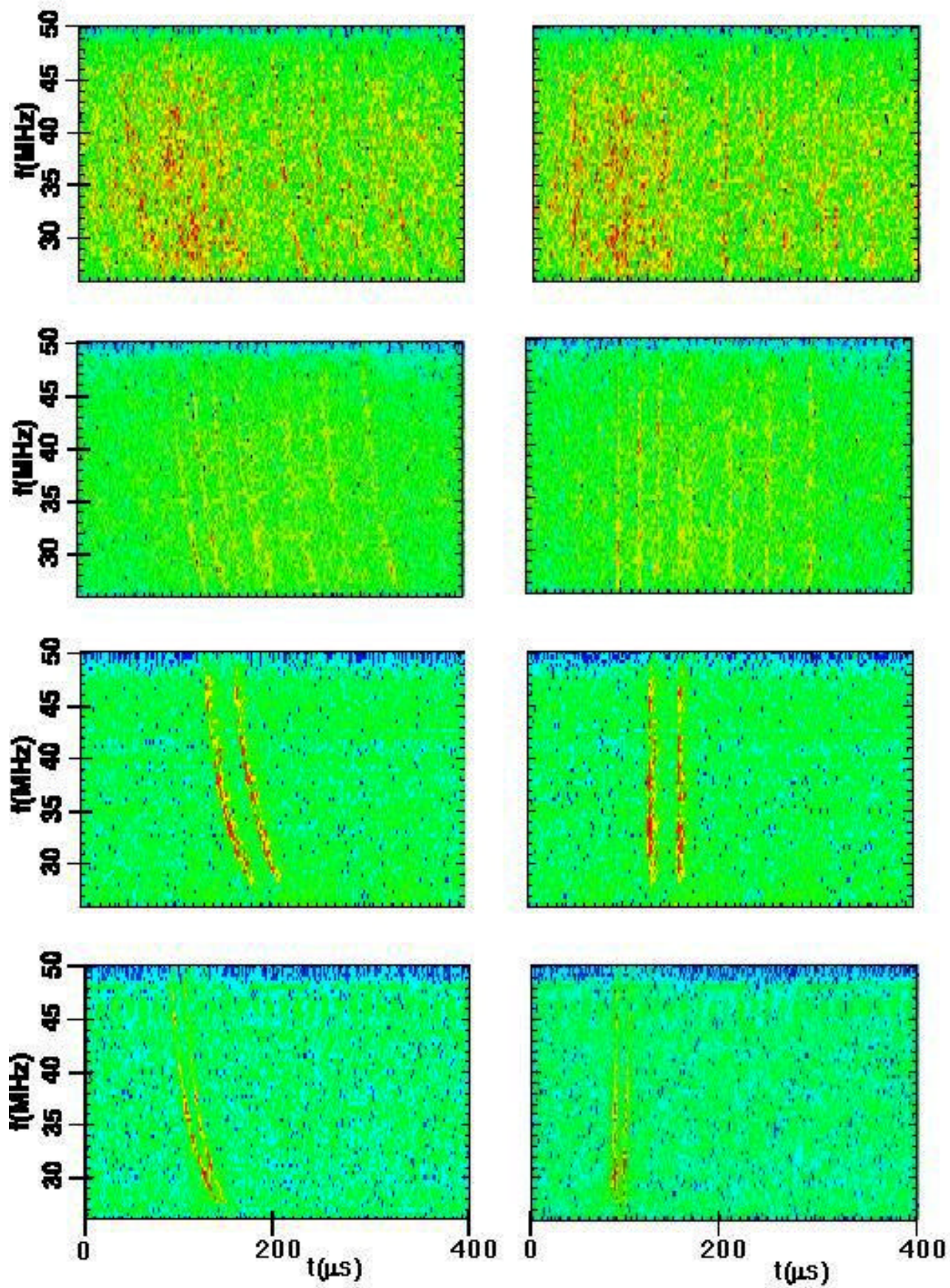
Figure 1: spectrograms of four exemplary lightning sigatures. Each spectrogram uses a 128-sample (2.56−μs) Fourier window advanced in 8-sample (0.16-μs) steps. The left column contains spectrograms in which carriers have been partially suppressed, while the right column contains the same spectrograms optimally dechirped. The optimal-dechirp inferred slant TEC is (top to bottom) 2.70, 2.77, 4.20, and 4.07 $X10^{17}$ m^{-2}. The pixel color codes the logarithm of the power in that time/frequency pixel. The red-through-green dynamic range is ~35 dB. The peak electric-field spectral density is displayed as red and is (top to bottom) $10^{-8.5}$, $10^{-7.5}$, $10^{-6.0}$, and $10^{-6.0}$ in units of $(volts/m)^2/Mhz$ at the antenna. Thus the two lower examples have 25 db more peak spectral density than the uppermost example. This illustrates the wide dynamic range of the trigger system.

shows the result of this exercise for each panel. This is implemented by scanning the slant TEC in twenty steps of $0.5X10^{17}$ m^{-2}, finding the optimum, then rescanning in the vicinity of the rough optimum in thirty steps of $0.03X10^{17}$ m^{-2}, and recording the slant TEC which best "dechirps" the traces.

The metric of success in dechirping the dispersed features into vertical (i.e., simultaneous at all frequencies) features is as follows: At each of the fifty trial values of N, we sum each spectrogram column and take the fourth power of that frequency-summed spectral intensity. This is in turn summed rightward (i.e., over time steps) to give the time-sum of the fourth power of the instantaneous intensity. The optimum TEC is that value which maximizes this time-sum of the fourth power of the intensity. Choosing a high geometric power of the dechirped intensity nonlinearly rewards the "right" TEC.

The right column of Figure 1 contains the dechirped spectrograms, using the optimum TEC for each of the four events. We now mention the "type" of event with reference to this right column, starting from the top panel. This top event is typical of diffuse lightning emissions in the VHF, containing many dispersed traces almost overlapping with each other, and with poor contrast between peak and median instantaneous intensity. The second panel is an example of more distinct and discrete pulses,

believed to correspond to recurrent leader emissions. The third panel shows an isolated pulse pair, superficially not unlike those seen by Blackbeard [*Holden et al.*, 1995; *Massey and Holden*, 1995]. The fourth (lowermost) panel shows another pulse pair, this time with shorter separation and with a disquieting (for TIPPs) hint of frequency-dependent separation.

We use the pre-whitened, de-chirped spectrogram (right side of Figure 1) as the basis of the event-sorting and data entry into a lightning-signature database. It is an empirical fact that within either the lo-band or the hi-band 22-MHz effective-width channel, the spectral structure does not seem to convey much information apart from ionospheric dispersion, which we successfully remove anyway. Put another way, all lightning VHF signatures we have seen with FORTÉ behave like incoherent emitters which are quasi-white-noise-like within either 22-MHz-wide channel. This applies equally well to the TIPPs (see bottom two panels in Figure 1) as to the diffuse emissions (see topmost panel) [*Massey and Holden*, 1995]. Given the lack of interesting spectral structure within a given channel's lightning signature, we may just as well compress the data by summing vertically (in frequency) to get the pre-whitened, optimally de-chirped power versus time. This is what we do.

Figure 2, top panel shows this power versus time (for the prominent TIPP from the third panel of Figure 1). Due to the 128-sample window advanced by 8 samples, the resolution in this plot is around 2 μs. The algorithm then examines the ratio of the peak to the median pre-whitened, optimally de-chirped power. This ratio is called simply the "contrast" of the signature. For the power curve in the example of Figure 2, the contrast is very high (=230). (By comparison, the contrast for the diffuse lightning of Figure 1's top panel is only 9.) We do not consider cases where the contrast is <3.
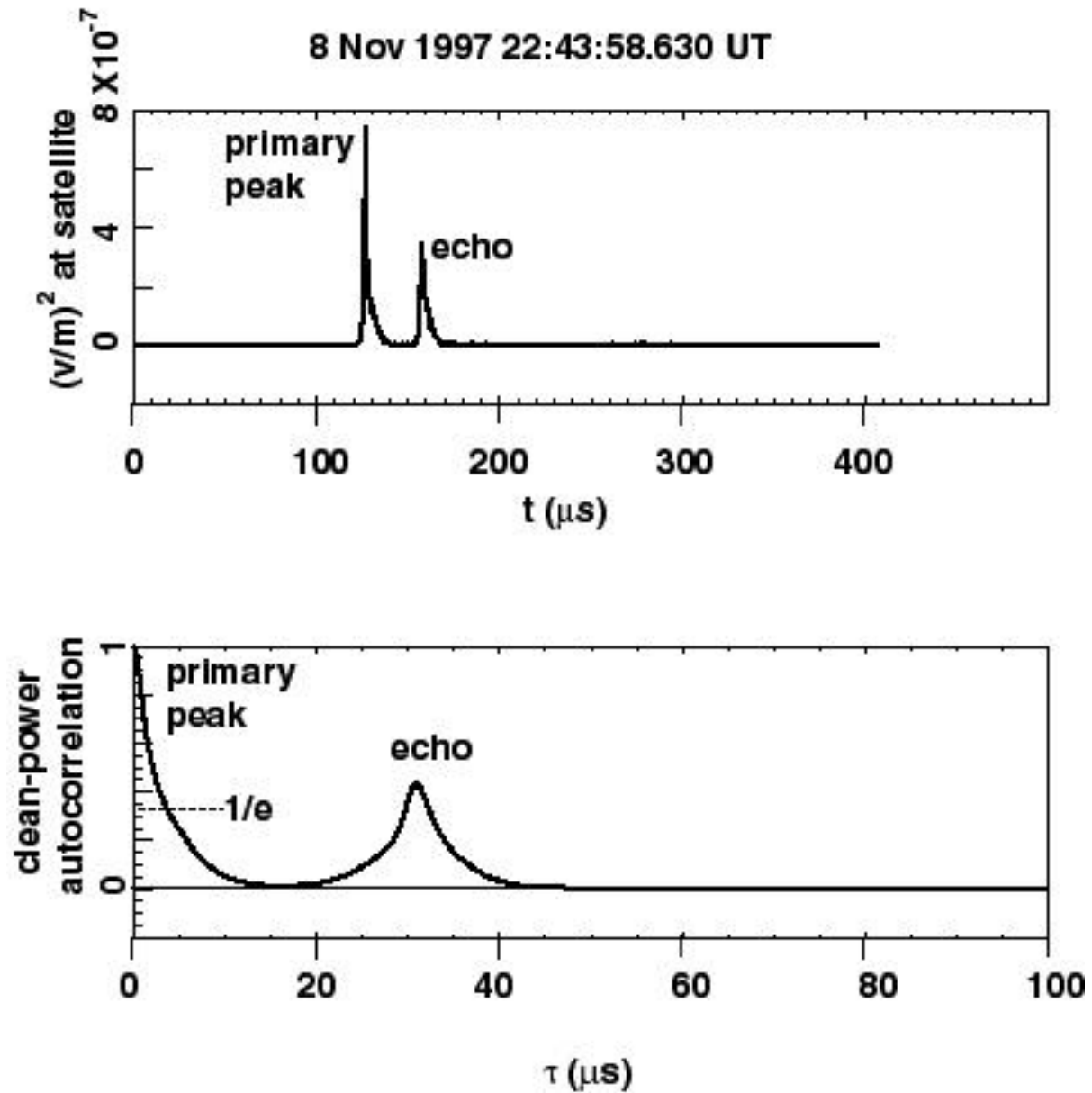
Figure 2: Power versus time (top panel) and normalized, lagged autocorrelation function (bottom panel) of the power. The power is from frequency-integrating the dechirped spectrogram's spectral density in the third panel of Figure 1.

The next step in the event-sorting is to calculate the lagged autocorrelation function of the pre-whitened, optimally de-chirped power. This is shown in Figure 2, bottom panel. The 1/e width of the central peak is 3.2 µs. Whenever the 1/e width is less than 10 µs, we procede to search for a secondary peak, or "echo". (The word "echo" implies no prejudice about what causes it, and only acknowledges that it comes later than the

main pulse.) If on the other hand the 1/e width exceeds 10 µs, we do not attempt to locate a second peak, because the feature is too diffuse to be useful in resolving that peak's lag.

We next examine the suitability of the echo in terms of signal-to-noise and resolution criteria: First, we examine the signal-to-noise ratio ("snr2") of the secondary echo, using as the denominator the rms fluctuation level in the correlation function far from the primary and secondary peaks. For this data in Figure 2, snr2=29. We do not procede any further if snr2<5, but if snr2 5, we note the echo lag. For this data, the echo lag is 30.7 µs.

We thus form a compact database containing both essential "housekeeping" parameters and derived quantities. The latter include (1) average pre-whitened, optimally de-chirped power, (2) peak pre-whitened, optimally de-chirped power, (3) optimal slant TEC, (4) power-autocorrelation 1/e width, (5) power-autocorrelation secondary-peak snr2, (6) and power-autocorrelation secondary-peak lag. These are stored for both of the 22-MHz effective-bandwidth channels, with the proviso that only the lo-band TEC is meaningful; the hi-band signal lacks enough dispersion to be sensitive enough in determining TEC.

4. General features of archive

The rest of this article describes the data gathered during the period 2 September 1997 through 12 April 1998, approximately 7 months of quasi-continual data. Figure 3 shows a histogram of the subsatellite latitudes at which triggered lightning records were recorded. The total number of records with contrast >3 is 478,468.The dataset through 12 April 1998 is biased toward tropical lightning, due in part to the season (completely lacking northern summer) in which the data were taken. This curve is in
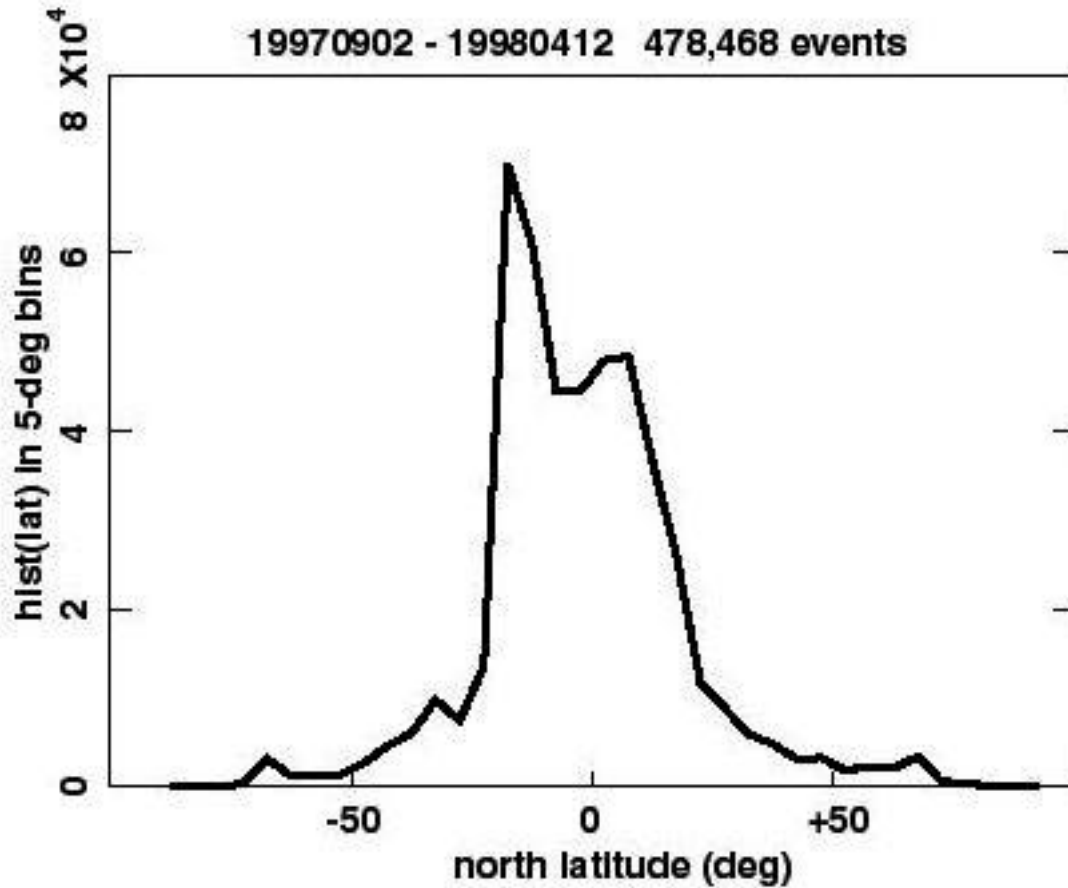
Figure 3: Histogram of subsatellite latitude for all 478,468 events having contrast >3. The heavy bias toward the tropics is because the first seven months of operation did not include northern Summer.

no way meant to reflect the *incidence* of lightning versus latitude, only that there are latitude-sampling biases in the FORTÉ database to date.

These same 478,468 events' contrast distribution is shown in Figure 4. The curve does not extend below contrast=3, because we do not let such events even enter the compact database. We have found that for data gathered after 27 October 1997, this is an adequate protection against contamination from on-board noise. Before that date, there is some contamination, and a higher threshhold requirement (contrast 8) is helpful for some of the earlier data.
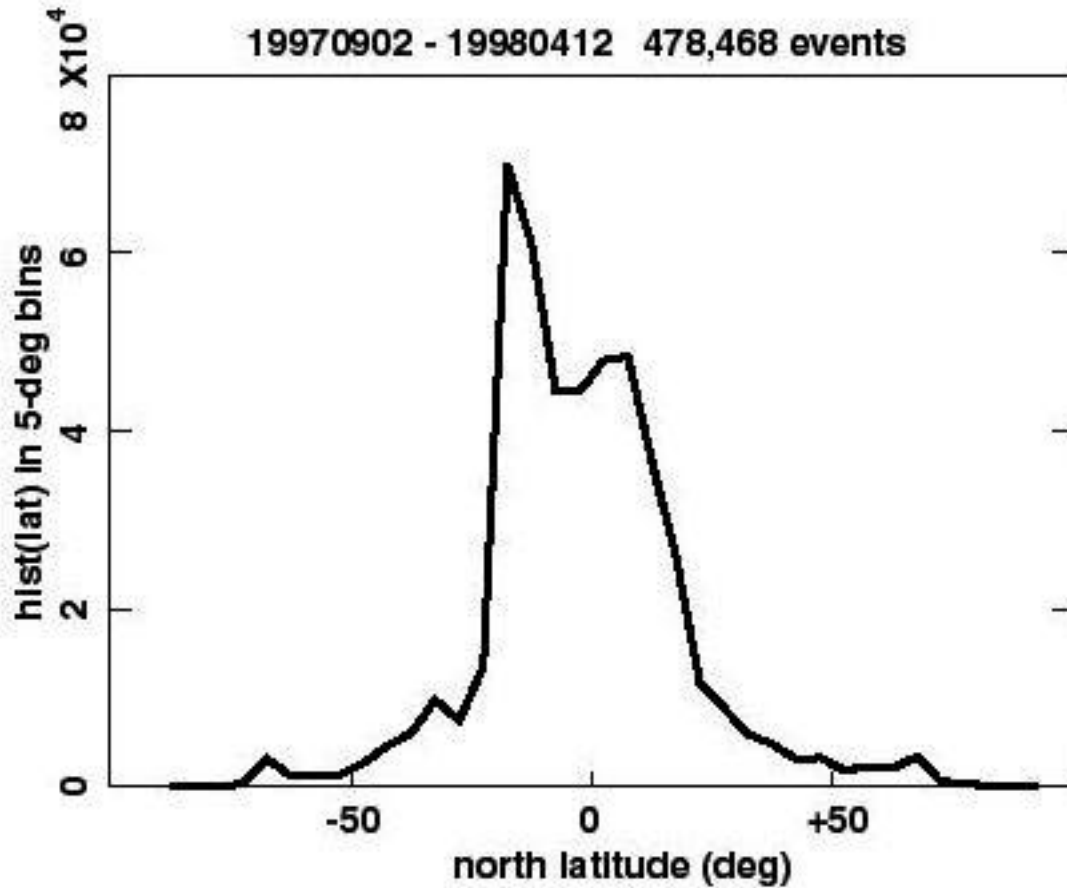
Figure 4: Histogram of peak-to-median ratio ("contrast") of pre-whitened, optimally dechirped power for all 478,468 events having contrast >3.

Restricting attention for the moment to the 114,662 pulse pairs with high contrast (>20) and high snr2 (>8), Figure 5 shows a histogram of their inter-pulse lag. The roll-off at and below 15 µs is not just a bias, but is real; the algorithm is unbiased at least down to 8 µs of lag. Similarly, the rolloff above 60 µs is real; the algorithm is capable of searching out to 150 µs, and does so. The FORTÉ intra-pulse-pair lag distribution thus confirms two key properties of the distribution seen earlier with Blackbeard [*Holden et al.*, 1995; *Massey and Holden*, 1995]. However, the detailed shapes of the distributions are not the same. We point out that this does not mean different physical phenomena are being observed by the two satellites. Rather, the FORTÉ trigger system's ability to acquire signatures which are weaker (compared to the man-made noise background) removes a bias that may have been operative in Blackbeard

toward large-lag signals (see explanation below in terms of ground reflection, in Section 5a).
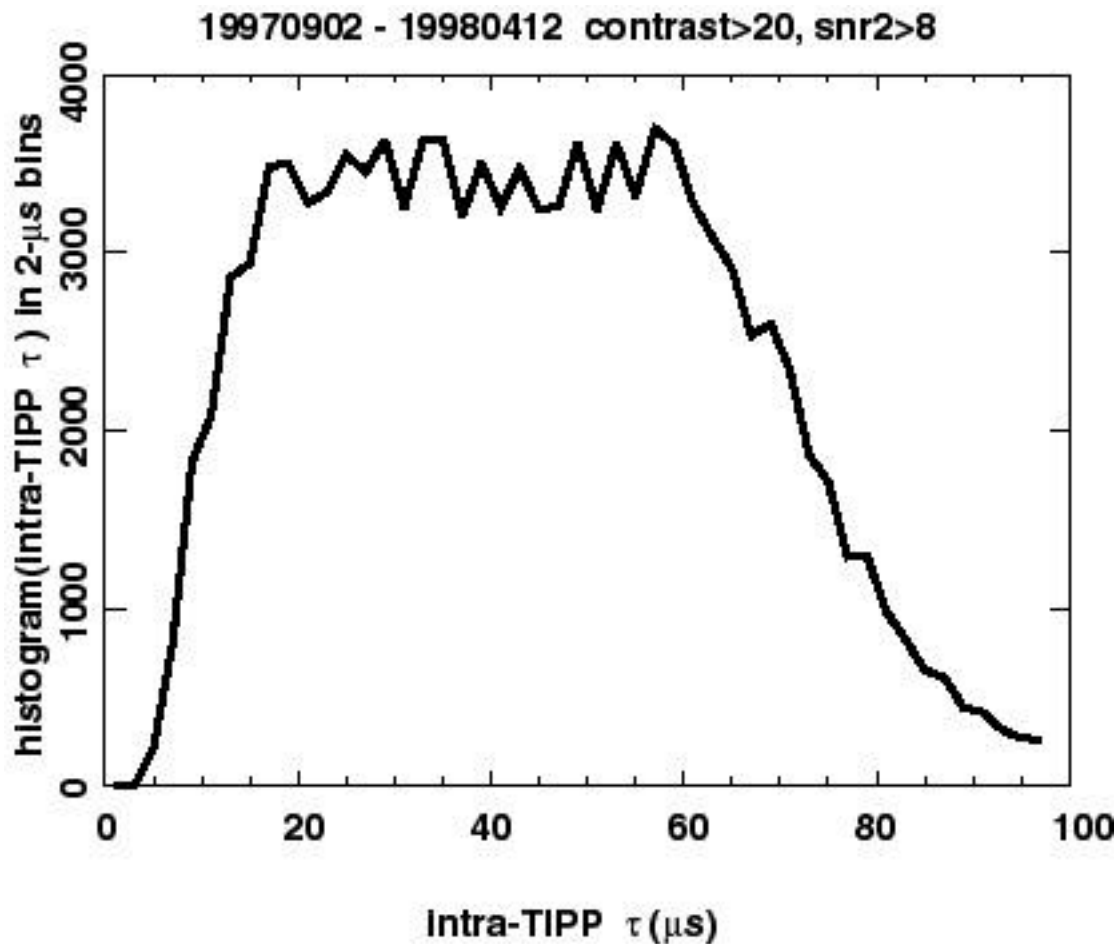

Figure 5: Histogram of inter-pulse separation for 114,662 "trans-ionospheric pulse pairs" (TIPPs) having contrast > 20 and snr2 > 8.

5. What causes the second pulse in a pulse pair?

5a. Background

The observation by Blackbeard of TIPPs [*Holden et al.*, 1995] instigated a lively discussion on the origin of the second pulse. Figure 6 serves to recapitulate the two alternative hypotheses. In each hypothesis, a tropospheric lightning process emitts prompt VHF along a direct ray to the satellite; this is the first pulse in the pulse pair.
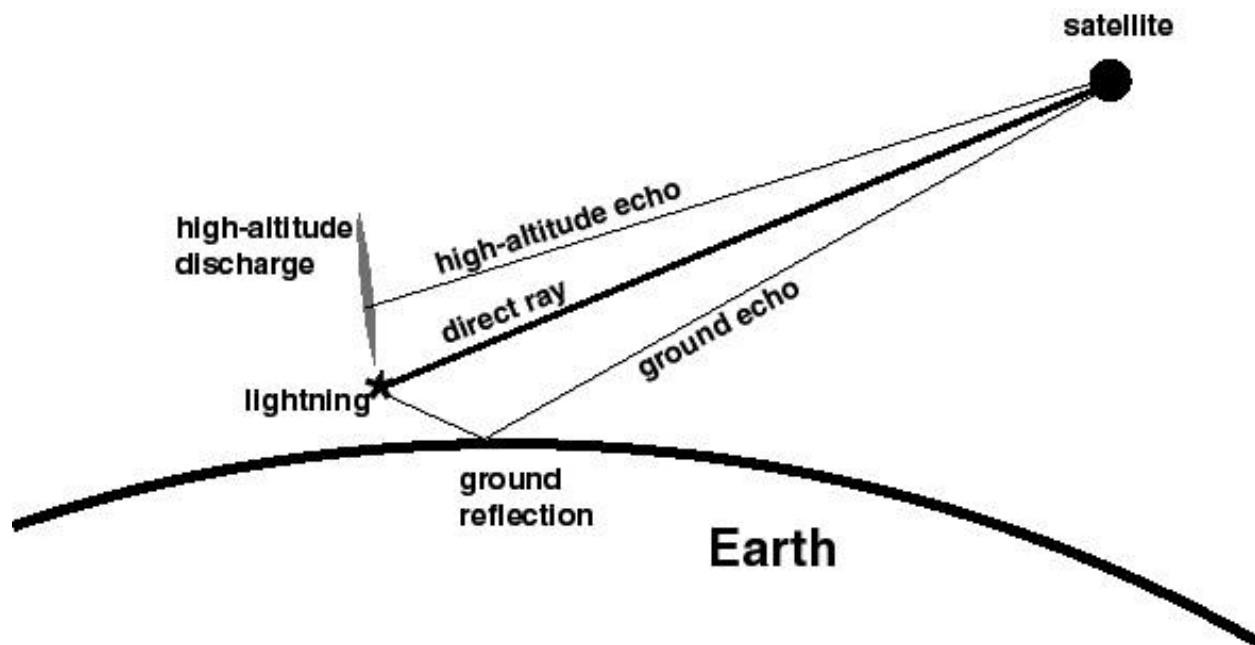
Figure 6: Cartoon of the two hypotheses on origin of a TIPP's second pulse, or echo. The high-altitude-discharge (HAD) model posits that the second pulse is from a secondary discharge in the mesosphere. The ground-reflection (GR) model posits that the second pulse is simply from a ground reflection.

The high-altitude-discharge (HAD) hypothesis [*Roussel-Dupré and Gurevich*, 1996] is based on the well-demonstrated fact that a relativistic upward discharge (eventually closing in the ionosphere) can be expected above thundercloud electrostatic transients in achievable storm-electrification conditions. The HAD paradigm for TIPPs explains the second pulse in a pulse pair as follows: There are really *two* breakdown regions, one near or in the cloud (radiating the first signal), and the second in the mesosphere, where, although the electric stress E is lower, the ratio E/P becomes large again (due to exponential decrease of p versus altitude). This second breakdown region is expected to radiate VHF, causing the second pulse. The breakdown-inducing electric stress from the cloud (site of the original transient) to the mesosphere propagates at nearly the speed of light. In Figure 6, the shaded region is the high-altitude discharge. It radiates an "echo" (i.e., late-arriving) pulse to the satellite. The delay of the echo pulse, relative to the primary pulse, is *maximum* when the satellite is low on the horizon, and is roughly given by (mesosphere height - cloud

height)/*c*, or perhaps 60 km/ (0.3 km/µs) = 180 µs. Moreover, the more typical observation geometry would be for the satellite closer to zenith. The HAD paradigm predicts that the lag would monotonically decline as the satellite approaches zenith, and would go to zero for the satellite directly at zenith (and for the electric-field-transient's vertical propagation at the speed of light). Thus, in terms of the observed lags, supplemented by no other information, the HAD hypothesis [*Roussel-Dupré and Gurevich*, 1996] is very successful.

The alternative, ground-reflection (GR) model [*Massey and Holden*, 1995; *Massey et al.*, 1998] maintains that the second pulse in a pulse pair comes simply from VHF reflection off the Earth's solid or water surface. This hypothesis is equally successful at reproducing the range of inter-pulse lags observed. The GR paradigm predicts that as the satellite approaches zenith (relative to the emitter), the lag will increase, maximizing at twice the emission height divided by c, and that the lag will approach zero as the satellite approaches the horizon (seen from the emitter).

Thus the two explanations for the origin of the second pulse give *qualitatively opposite predictions on the dependence of inter-pulse lag on satellite zenith angle* (relative to the first-pulse emitter). Unfortunately, stand-alone pulse-separation measurements do not permit the zenith angle, or even trends in the zenith angle, to be unambiguously resolved. Thus the Blackbeard data could not *definitively* resolve the HAD/GR paradigm choice.

5b. Correlated behavior of TIPP-lag and slant-TEC statistics

The ability of FORTÉ to acquire copious records and to determine the slant TEC from each record allows us to throw new light on the origin of the echo in TIPPs. The slant TEC should be a monotone-increasing function of satellite zenith angle (as seen from the emitter), all other things being equal. Thus if we find a systematic relationship

between slant TEC and TIPP inter-pulse separation, we can resolve the competition between the HAD and GR hypotheses for the origin of the second pulse.

The ionosphere, even the mean climatological ionosphere, varies versus latitude, local time, day of year, and sunspot number, as well as in a more complicated way with geomagnetic activity. Thus, any correlation between TIPP inter-pulse lag and inferred slant TEC is likely to be significantly blurred, though perhaps not altogether obscured, by these other variables.

In order to control at least partially for local time, we can choose windows centered on both local noon and local midnight, the expected local-time stationary points of the ionospheric diurnal climatology. Figure 7 shows a barchart of median slant TEC for 6-hour local-time windows centered on both noon (solid curve) and midnight (dashed curve). (The barchart as used here is a statistical display of one parameter's value in bins of other parameters.) Because the data through 12 April 1998 were biased toward dawn/dusk, there are only 7,321 TIPPs at local noon (the period of our sparsest coverage), and only 25,678 TIPPs at local midnight. Within each bin of intra-TIPP lag, Figure 7 shows the median value of the slant TEC as derived from optimal de-chirping of the lo-band spectrogram. The first thing to note is that there is a three-fold enhancement of slant TEC at noon over midnight. The second thing to note is that in each 6-hour epoch, there is a modest decrease of median slant TEC with increasing intra-TIPP lag. This is consistent with the GR model, and contrary to the HAD model.
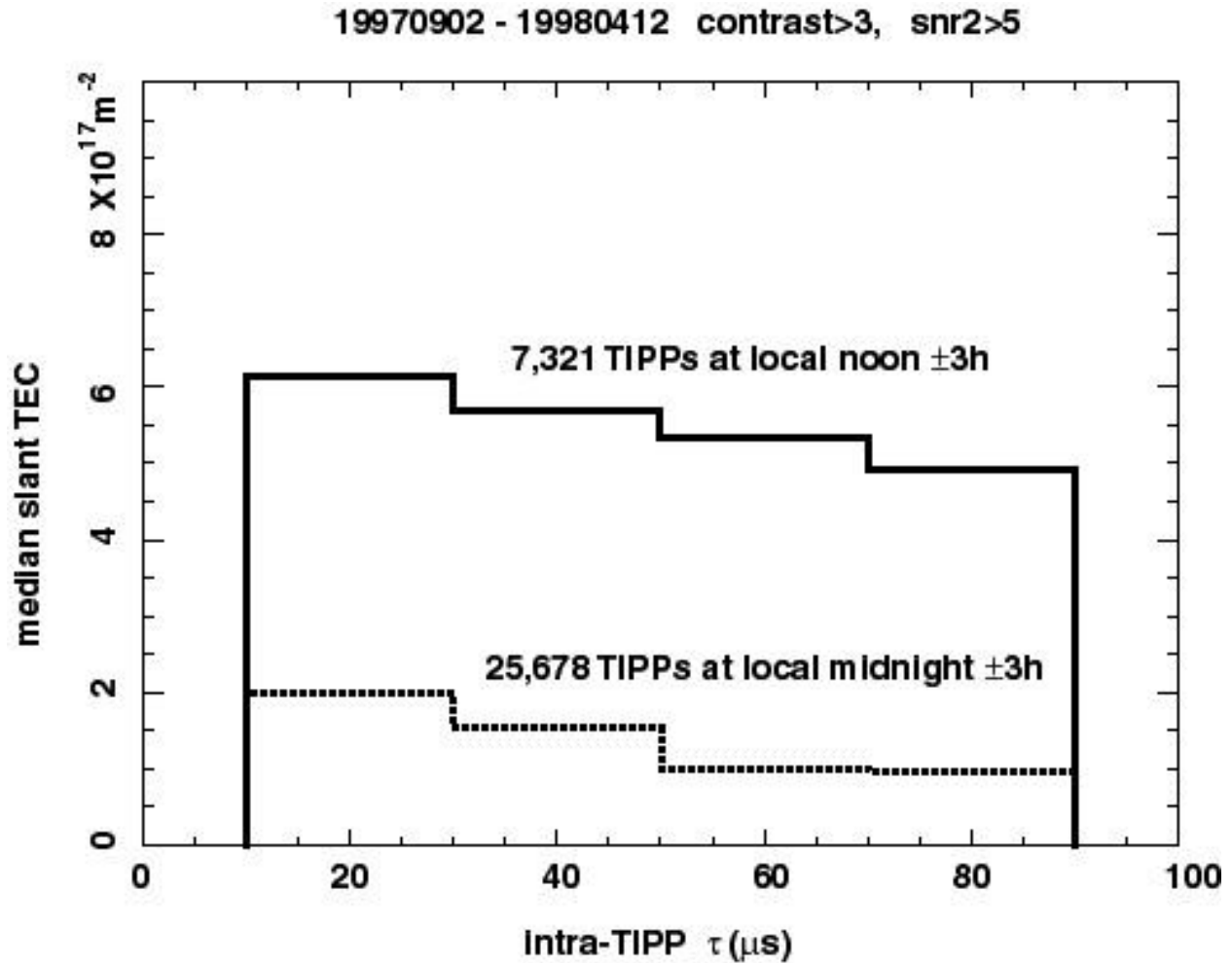
Figure 7: Barchart of median lo-band-inferred slant TEC for 6 h around local noon (solid) and local midnight (dashed), using TIPPs with contrast > 3 and snr2 >5. The barchart abscissa is the intra-TIPP separation, binned in 20-μs groups.

5c. Evidence of recurrent-emission storms: qualitative behavior

Cleaner and more compelling evidence from the slant-TEC correlation with intra-TIPP lag is found in the case of recurrent-emission storms. Such storms, in fact, furnish almost all of our FORTÉ observations of TIPPs. What happens is as follows: Any point in the lower atmosphere is continuously visible for an extended time (>15 minutes for satellite track directly overhead) during a FORTÉ overflight at 800-km altitude. This allows a VHF emission center in the storm to radiate to FORTÉ recurrently, both many times within one flash, and in recurring flashes (for time-clustering statistics, see Section 6 below).

The FORTÉ observations of TIPPs from such storms are typified by Figure 8, showing a passage over the Gulf of Mexico and the southeastern United States during 10 minutes around 02: UT on 8 April 1998 (local evening). The top panel shows the intra-TIPP lag, with square symbols for lo-band and diamond symbols for hi-band lag determinations. The two symbols overlap very closely, indicating close agreement between the lag estimations in the two VHF bands observed. The lower panel in Figure 8 shows the corresponding inferred slant TEC. This is shown only for the lo-band data, as the TEC determination above 100 MHz is of questionable sensitivity and is not even attempted in forming the compressed database. The two curves have complementary trends, the TIPP curve being convex upward, and the TEC curve being concave upward. Moreover, the two curves attain their extrema at about the same time. This is a typical FORTÉ storm-overflight picture of the intra-TIPP lag and TEC data for recurrent emitters. We have accumulated well over a thousand such recurrent-storm overflights in just seven months, and in all cases the same TEC/lag complementarity is observed. We are unaware of even a single exception.

What does Figure 8 say about the two second-pulse hypotheses? The HAD hypothesis would predict that *both* intra-TIPP lag, and slant TEC, would *together* increase as the satellite goes to either horizon, and would *together* decrease as the satellite approaches the zenith. In other words, both curves should be convex-downward if the HAD hypothesis is valid. We do not see that behavior at all in the data. We are unaware of even a single exception to this rule. By comparison, the GR hypothesis predicts the complementary trends we see qualitatively in Figure 8 and in all other overpass data involving recurrent-emitter TIPPs.
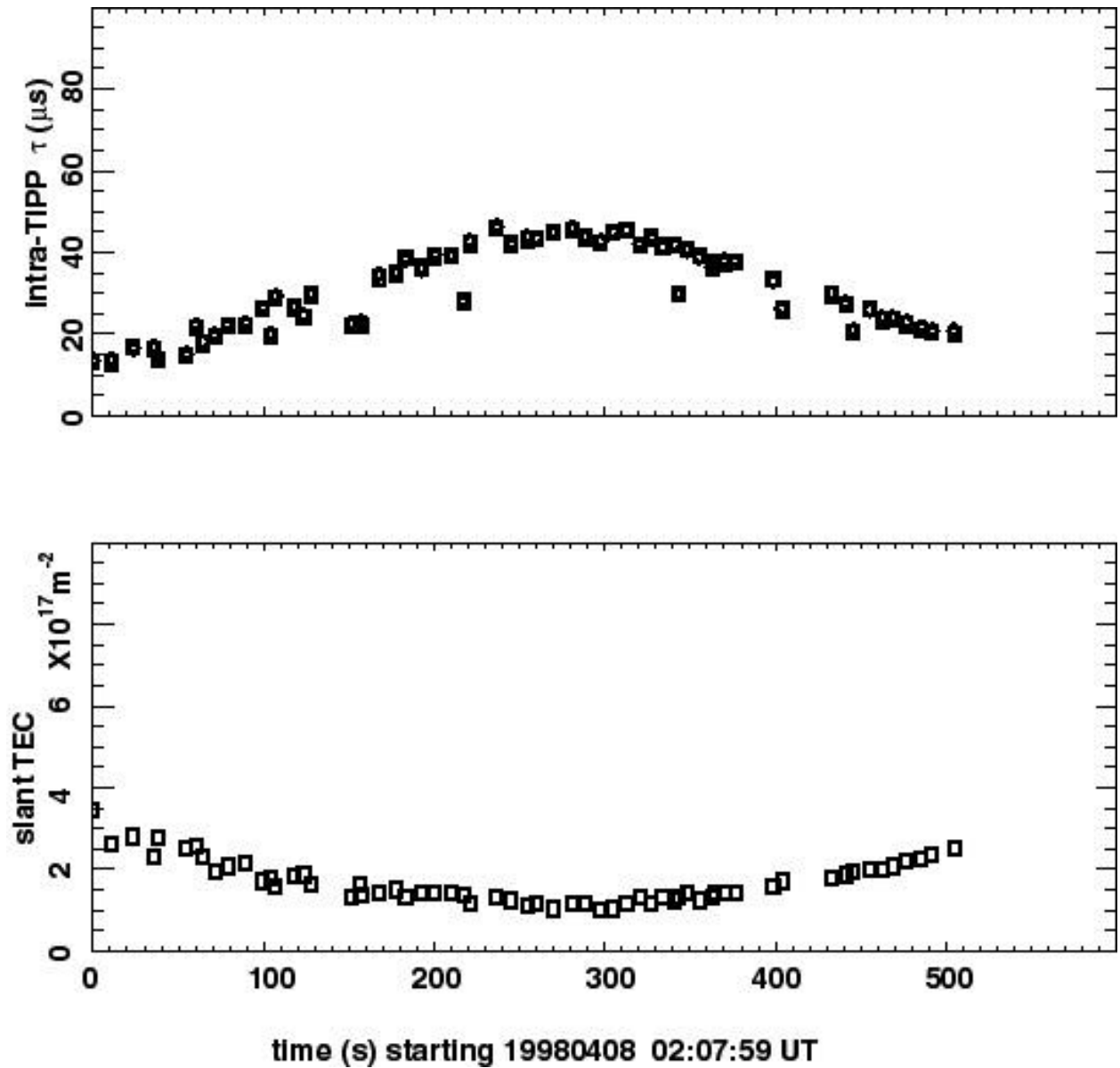
Figure 8: Intra-TIPP separation (top panel) and lo-band-inferred slant TEC (bottom panel) versus time for a pass near a recurrent-emitter storm. In the top panel, the squares are for lo-band, and the diamonds are for hi-band.

5d. Recurrent-emission storms: quantitative analysis

This section predicts more quantitatively the implications of the GR model on the intra-TIPP lag, both to further illuminate the choice between the HAD and GR hypotheses and to set the stage for approximate geolocation of recurrent-TIPP storms (which will be systematically presented in future publications). Figure 9 shows the geometry. A VHF emitter ("e") is located in the lower atmosphere, at height a above the ground. A
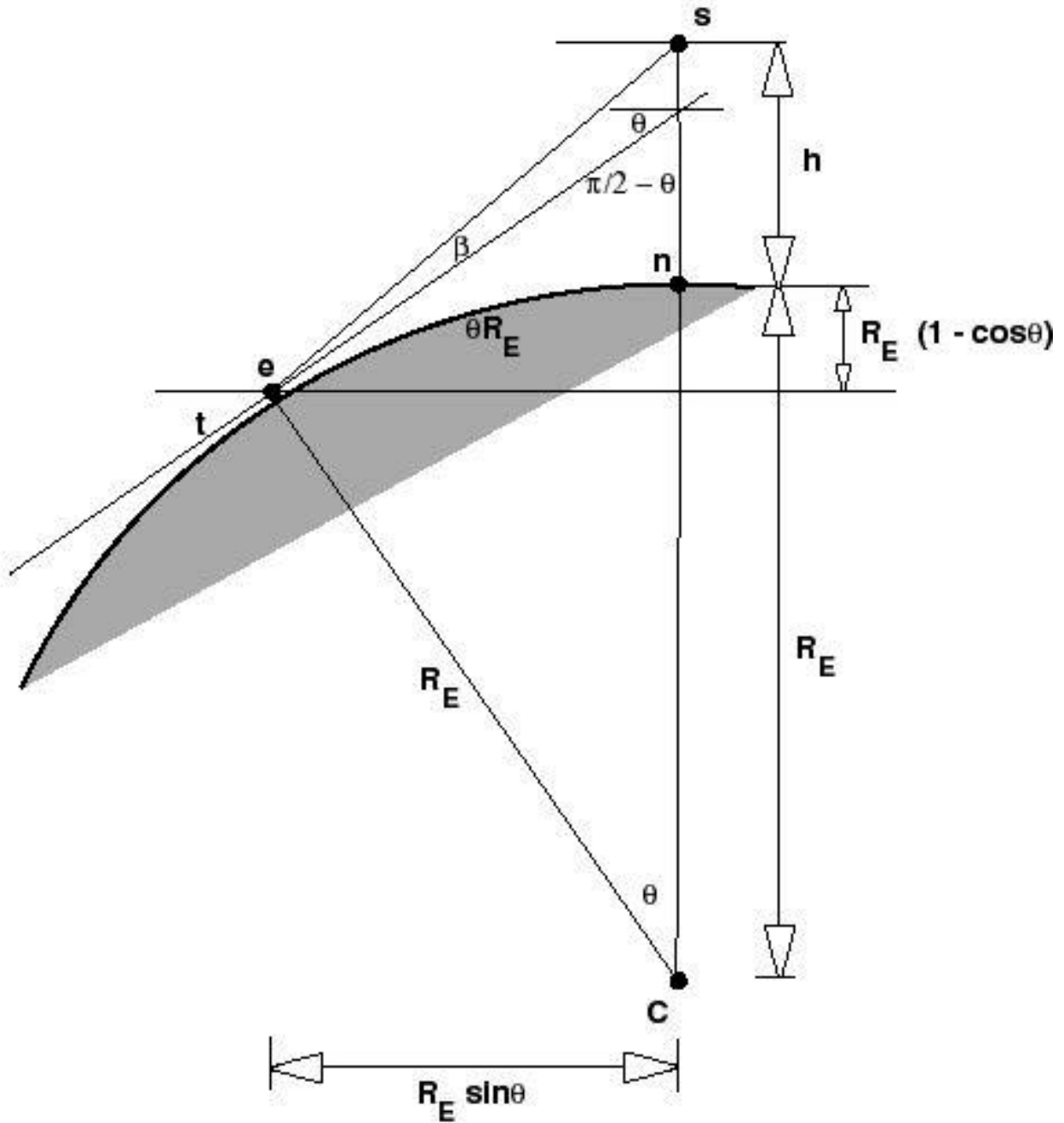
Figure 9: Geometry of satellite (*s*), subsatellite nadir (*n*), and VHF emitter (*e*) relative to the Earth (shaded).

satellite ("*s*") is at an altitude *h* above its nadir point on the ground ("*n*"). The angle between *n* and *e* is . The arclength on the surface of the Earth, between *n* and *e*, is R_E, where R_E is the Earth radius. In the following we will assume both that $a <\!< h$ and that $^2 <\!< 1$. The former is guaranteed by the fact that the troposphere extends only to

~15 km, while the satellite is at ~800 km. The latter is also true, because the very horizon seen by FORTÉ is at only θ_{max} = 0.5 radian, and most of the data we treat will be from emitters much closer than the horizon.

From the emitter, the satellite elevation angle is ϵ. Figure 9 shows that

$$\tan\left(\epsilon + \theta\right) = \frac{h + R_E\left(1 - \cos\theta\right)}{R_E\sin\theta} \tag{2}$$

from which it follows that

$$\epsilon = a\tan\left\{\frac{h + R_E\left(1 - \cos\theta\right)}{R_E\sin\theta}\right\} - \theta \tag{3}$$

Now consider the surface of the spherical Earth as shown in Figure 10. The instantaneous angular distance from the satellite nadir to the emitter is θ, and the satellite is an angular distance l from its closest approach to the emitter. At closest approach, the angular distance from the subsatellite point to the emitter would be m. The spherical-geometry version of Pythagoras' theorem states

$$\cos(\theta) = \cos(m)\cos(l) \tag{4}$$

which in our approximation gives
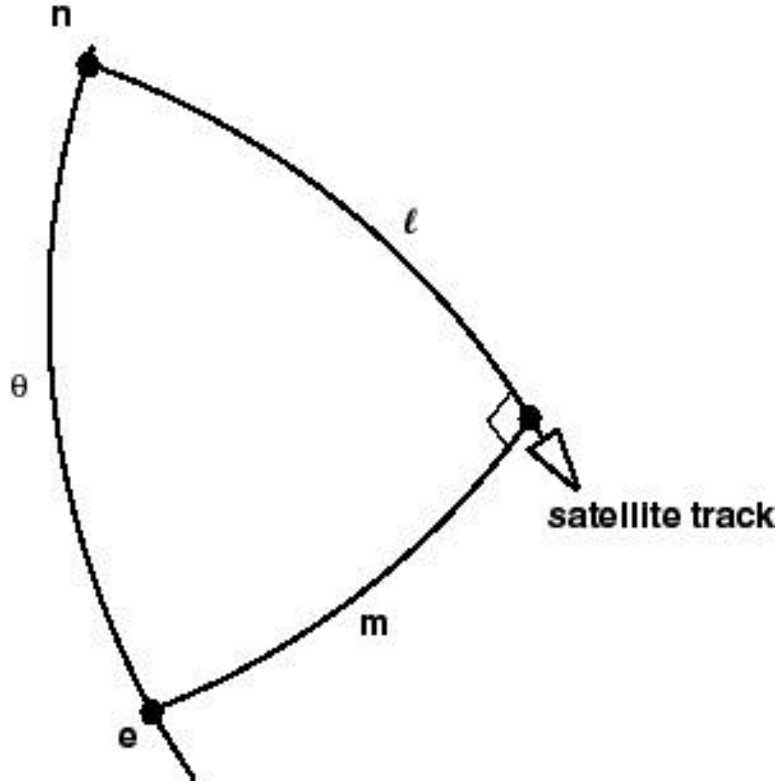
$$\theta^2 = m^2 + l^2 \tag{5}$$

Figure 10: View of subsatellite track, great-circle arc from nadir (*n*) to emitter (*e*), and great-circle arc from emitter to point of nearest approach of satellite, on the curved surface of the Earth.

Combining Eq. (5) with Eq. (3) leads to

$$\text{atan}\left\{\frac{h + R_E\left(\dfrac{m^2 + l^2}{2}\right)}{R_E\sqrt{(m^2 + l^2)}}\right\} - \sqrt{(m^2 + l^2)} \tag{6}$$

Figure 11 shows the emitter, the nearby ground, and the putative reflection off the ground. Because the satellite distance from the emitter is very large compared both to *a* and to the distance *p* from the emitter to the reflection point, we may assume to first order that both the direct ray to the satellite, and the echo ray from the reflection to the satellite, are parallel to each other. Thus, from the reflection point, the satellite elevation angle is still just . The additive distance from the emitter to the satellite traveled by the reflected echo, relative to the direct path, is *p-q*. From Figure 11, we have
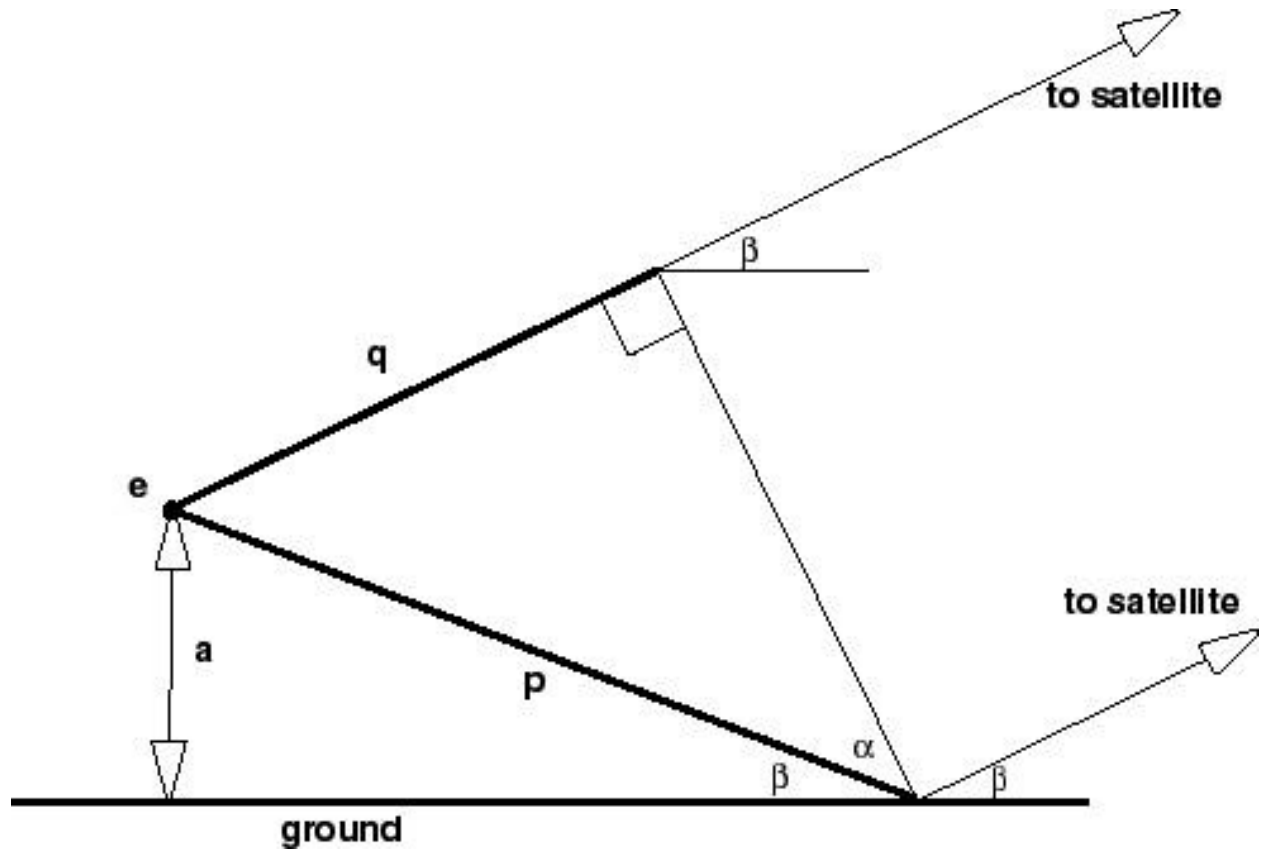
Figure 11: Vertical-plane detail VHF emitter (*e*), the ground-reflection point, and the two quasi-parallel signal paths to the distant satellite. The differential path length is *p-q*.

$$p = \frac{a}{\sin}$$

(7)

and

$$q = p \sin = p \cos(2)$$

(8)

from whence

$$p - q = \frac{a}{\sin}\{1 - \cos(2)\}$$

(9)

Letting   be the intra-TIPP separation, we can finally write the equation for the emitter height, *a*:

$$a = c \ \frac{\sin}{1 - \cos(2\,)}$$

(10)

where *c* is the speed of light.

This equation is useful if we know the horizontal location (latitude and longitude) of an emitter, say by coincidence with ground-based sferic arrays, and wish to derive the emitter altitude from the intra-TIPP separation, in the GR hypothesis. However, in the case of recurrent-emitter overflights where separate geolocation information is unavailable (see Figure 8), we do not know *a priori* the emitter's horizontal location, so we cannot use Eq. (10) straightforwardly. Instead, we recognize that Eq. (10) describes a family of curves corresponding to different miss distances, that is, to different arc-separations from the emitter at closest approach by the satellite. Even when each curve is *normalized to its own peak value*, the various curves have different shapes, in a manner that varies monotonically with miss distance. For the satellite path being directly over the emitter (miss distance = 0), the curve's normalized curvature is strongest, while for the satellite being almost on the horizon at closest approach (miss distance approaching the radius of the horizon small circle, or 3200 km), the normalized curvature is weakest.

Figure 12 shows the *separately normalized* theoretical curves from inverting Eq. (10) to get   in terms of . The curves are for miss-distances (at closest approach) of 0, 600, 1400, and 1800 km. Superimposed on these curves are the recurrent-emitter lag data from Figure 8. It appears that the data are credibly contained under the curve for miss-distance of 600 km, and that the theory is capable at least of excluding either 1800 km or 0 km. The presence of some data well below the curve would correspond to VHF

radiation from lower altitudes than the capping altitude for emissions from that storm.

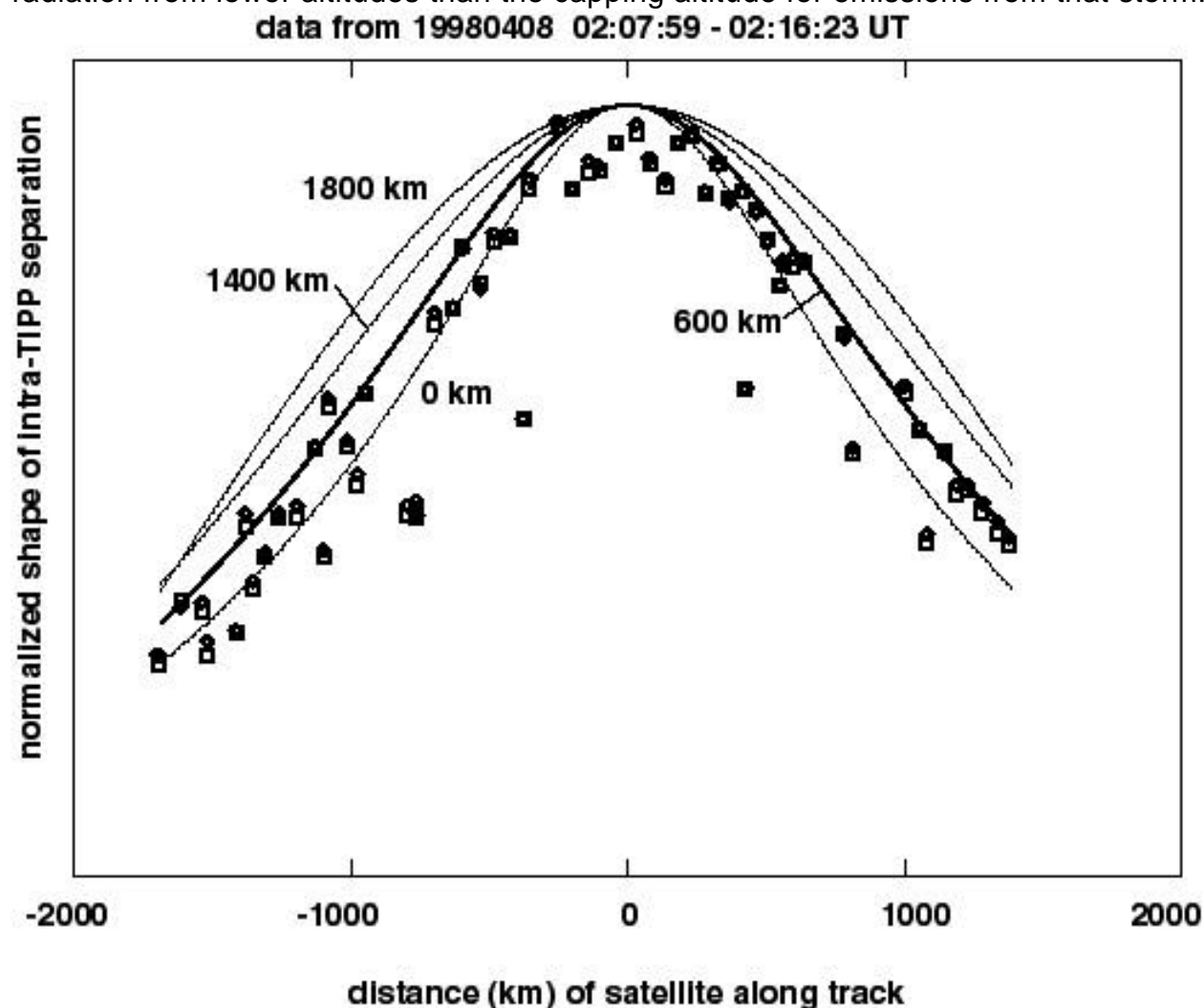
data from 19980408 02:07:59 - 02:16:23 UT

Figure 12: Intra-TIPP separation versus time (relative to time of nearest approach) for the recurrent-emitter storm of Figure 8. The data are shown as symbols, while the normalized curves are the model (see Eq. 10) for miss-distances noted.

The only attempt of the theoretical curves in Figure 12 is to match the data arising from discharges *at the capping altitude.*

5e. Hi/lo-band discrepancy on intra-TIPP lag

The treatment so far approximated that the ground-reflected echo ray (in the GR hypothesis) and the direct ray from the emitter are parallel. For grazing reflection off the ground, such as would occur in the GR hypothesis when the satellite is low on the

horizon (see from the emitter), we can refine the comparison of the GR hypothesis with the data. Figure 13 shows the same as Figure 11, but now we include the detail that the two rays (direct and ground-reflected) must converge at the satellite. For the satellite being low on the horizon, the distance to the satellite will be on the order of the miss-distance, while the inter-ray separation at their base will be on the order of a, so the convergence angle will be on the order of, and greater than, $a/(R_E)$. This leads the ground-reflected echo to have a steeper, and hence shorter, path through the ionosphere, compared to the direct ray. According to Snell's Law, this difference in ionospheric pathlength will be more pronounced, the lower the satellite is to the horizon (as seen from the emitter). This will lead to a difference between hi-band and lo-band intra-TIPP lags, a difference we now refer to as "defect".
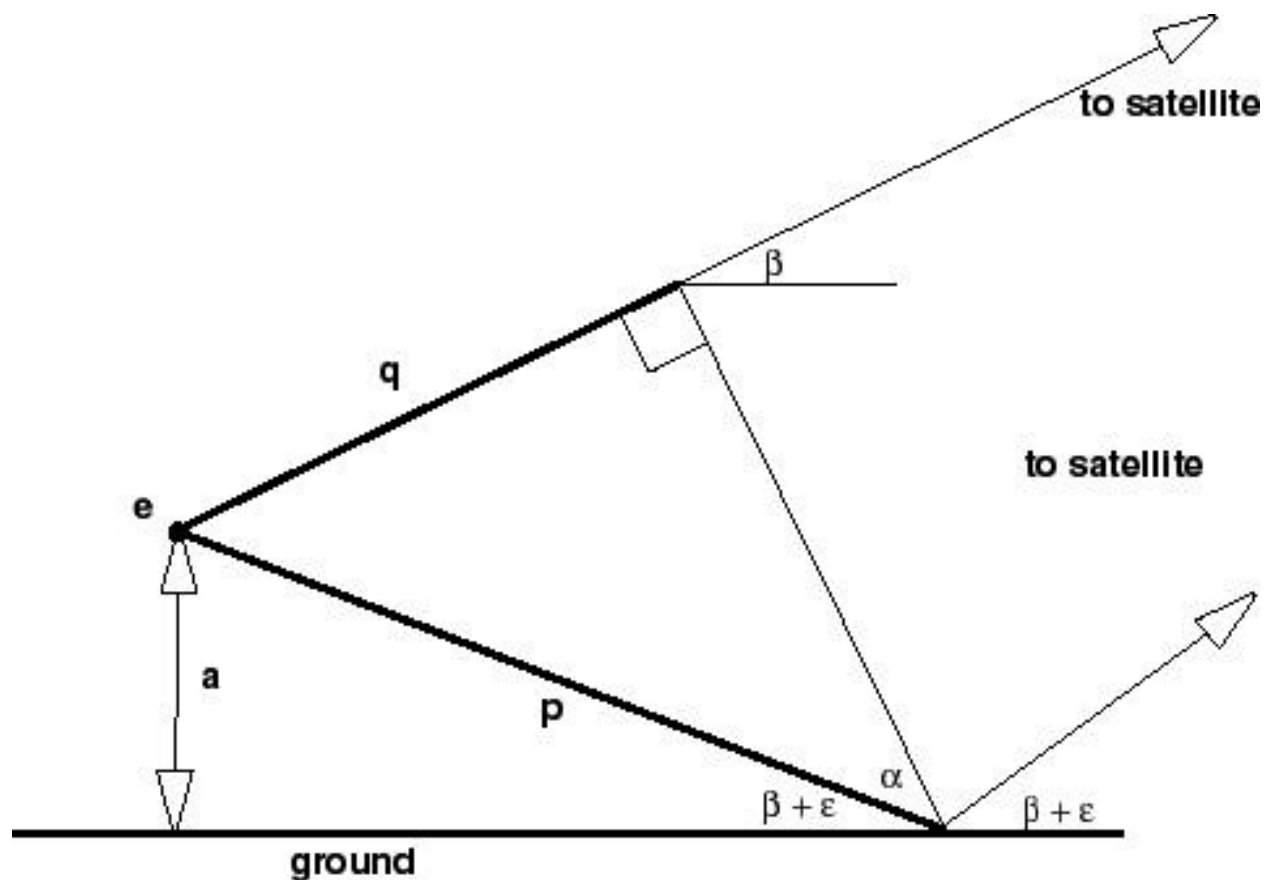

Figure 13: Similar to Figure 11, but now indicating the convergence (toward the satellite) of the direct and ground-reflected rays.

This effect predicted by the GR hypothesis becomes more extreme taking account of (1) spherical geometry and (2) raybending at the ionosphere/vacuum interfaces, as shown in Figure 14. For the satellite at zenith, the difference in ionospheric path length is zero, while for the satellite at low elevation angle, the raybending effect would be maximum. Similarly, for low mean TEC (nighttime ionosphere), the effect would be minimum, while for a full ionosphere, the effect would be maximum. By comparison, the HAD hypothesis has the secondary pulse taking a more oblique, and hence longer, path through the ionosphere (see Figure 8), relative to the direct ray, precisely the opposite of the GR hypothesis.
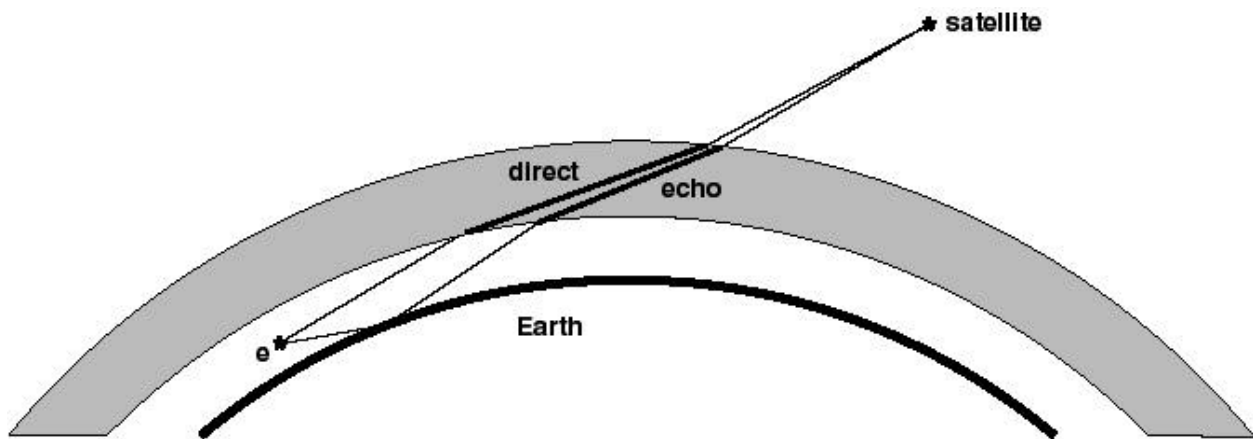

Figure 14: Cartoon of different ionospheric paths of direct ray and ground-reflected echo in the ground-reflection hypothesis. Raybending in the presence of a spherical ionosphere causes the ground-reflected path to be steeper and shorter through the ionosphere, relative to the direct path.

A longer path through the ionosphere means (all other things being equal) more slant TEC and hence a greater TEC-induced relative delay of the lo-band channel with respect to the hi-band channel (see Eq. 1 above). Thus if the GR hypothesis is correct, we would expect TIPPs to have somewhat shorter intra-TIPP lags at low band than at high band, while if the HAD hypothesis is correct, we would expect the opposite. In either case, we would expect the effect's magnitude to increase both with (1) denser ionosphere and (2) more oblique geometry (i.e., satellite lower on the horizon.)

We now recall the bottom panel of Figure 1. The lo-band TIPP signature in that spectrogram shows narrowing of the separation between the two pulses as the frequency goes down (from 50 down to 30 MHz), even within the lo-band bandwidth. For that particular event, the lo-band gross intra-TIPP separation (determined by the frequency-integrated power's autocorrelation function) is 10.1 µs, while that of the hi-band channel (not shown) is 14.2 µs.

Next, we examine the trends in this effect during an overpass by FORTÉ in which 35 TIPPs from a recurrent-emitter storm were observed during 250 s. Figure 15 shows the intra-TIPP lag (top panel) and lo-band-inferred slant-TEC (lower panel) in a format similar to that of Figure 8. In this case, however, there is a clear trend for the hi-band lag (diamond symbol) to exceed the lo-band lag (rectangle symbol), and moreso at the left end of the curve than at the right. Figure 16 shows the actual lo- and hi-band power autocorrelation functions of the event on the extreme left of Figure 15, to indicate the robustness of this measurement. The left end of Figure 15 (containing higher values of slant TEC) is clearly for the satellite's being low on the horizon, while the right end of Figure 15 (containing lower values of slant TEC) must be for the satellite being near to closest approach (to the storm). Thus the observed hi/lo defect in intra-TIPP lags is in the sense predicted by the GR hypothesis, and not in the sense predicted by the HAD hypothesis.

Extending the test of the hi/lo defect in intra-TIPP lag, we now examine statistically all the TIPPs in the database having contrast > 3 and snr2 > 5. Figure 17 shows four barcharts of the hi-band lag minus the lo-band lag. Each barchart is for a different range of mean intra-TIPP separations. Then, in each barchart, we plot the median hi minus lo defect in nine bins of lo-band-derived slant TEC. We make three observations:
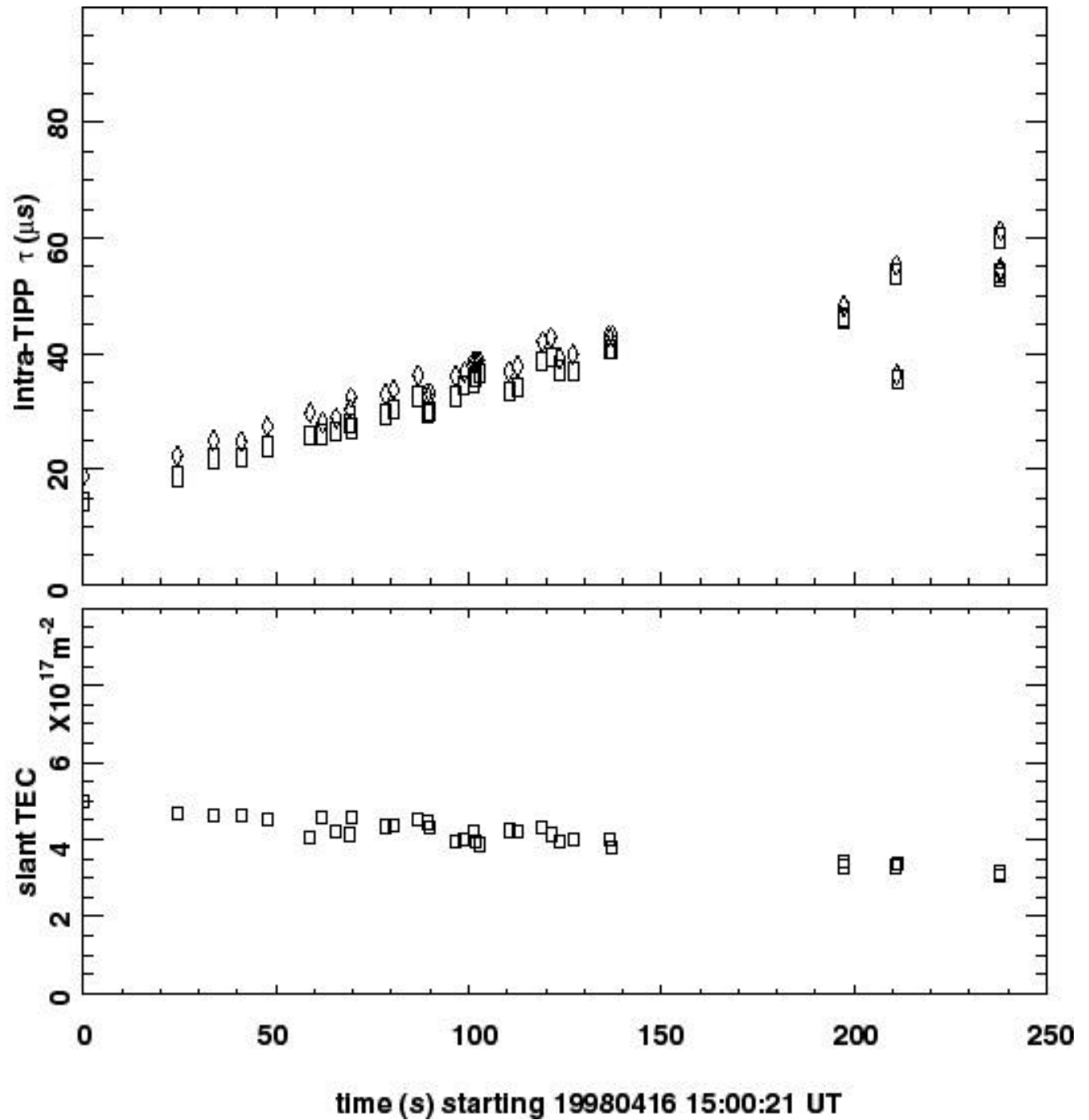
Figure 15: Intra-TIPP separation (top panel) and lo-band-inferred slant TEC (bottom panel) versus time for a pass near a recurrent-emitter storm lower on the horizon, and with more slant TEC than in Figure 8's storm. In the top panel, the squares are for lo-band, and the diamonds are for hi-band. The systematic difference between these two determinations of intra-TIPP separation is maximum at the left end of the diagram, where the satellite is lowest on the horizon (seen from the storm) in the GR hypothesis.
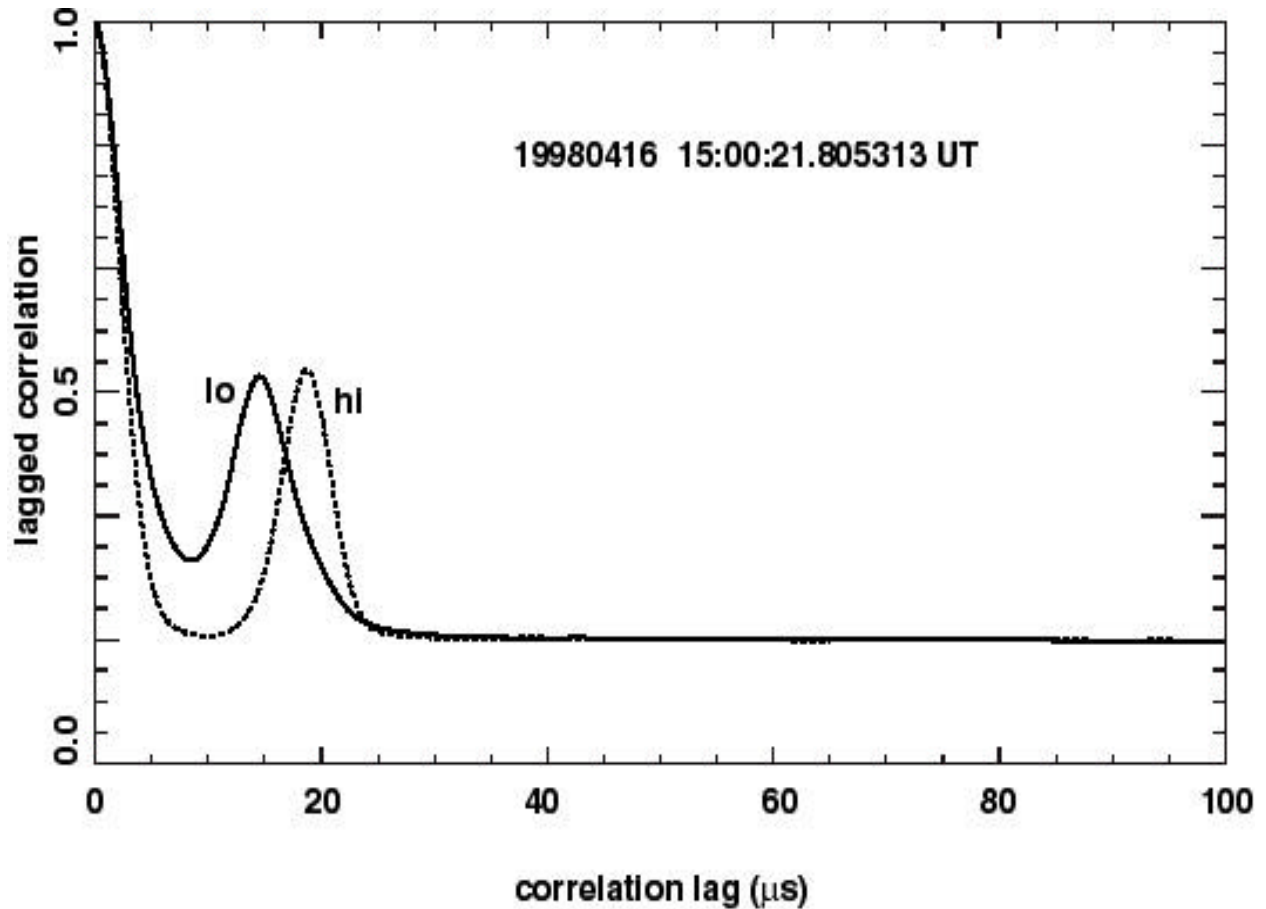
Figure 16: Comparison of lo-band (solid) and hi-band (dashed) lagged power autocorrrelations functions for the leftmost event in Figure 15, showing the robustness of the determination of the systematic difference in intra-TIPP lag.

 (1) The median defect in *all* TEC bins, and in *all* mean-lag groups, is positive. The result had been in no way assured *a priori*; and the positive sign of all the results is significant and telling, as the sign is consistent with the GR hypothesis and inconsistent with the HAD hypothesis.

(2) The defect is greatest for the shortest mean-lag group (upper-left barchart) and smallest for the longest mean-lag group (lower-right barchart). This is consistent with the GR hypothesis and inconsistent with the HAD hypothesis.

(3) Within each barchart, the defect increases for increasing slant TEC. This is consistent with either hypothesis and is a tell-tale of the controlling role of ionospheric refraction.
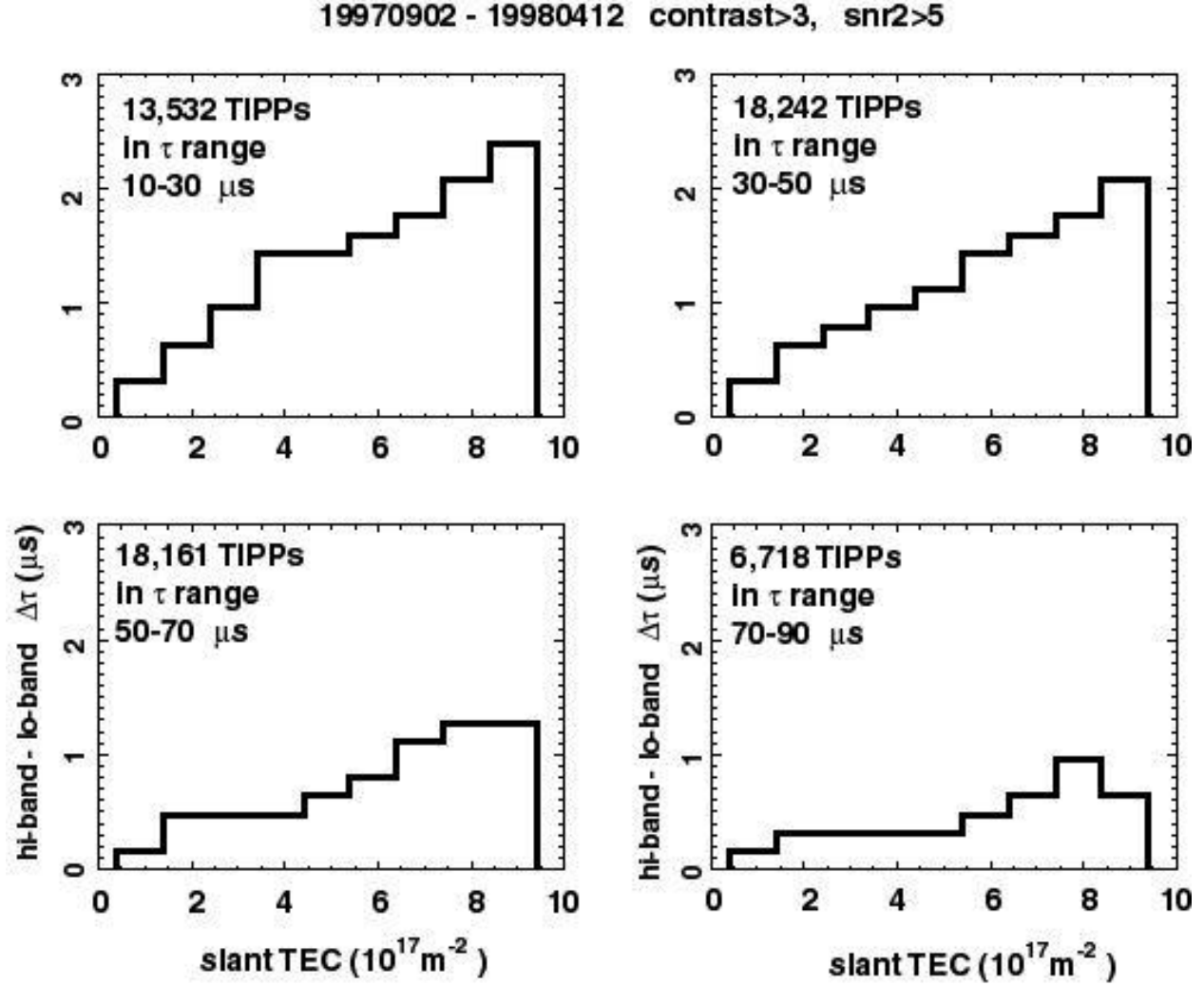
page 31

Figure 17: Barchart of median hi-band minus lo-band intra-TIPP separation difference ("defect" for short) for TIPPs with contrast > 3 and snr2 > 5. Each barchart represents a different subgroup, based on range of mean intra-TIPP separation. The barchart shows the median defect in each of nine bins of slant TEC.

In Figure 18, we look at the defect data differently, grouping the barchart populations into four groups of slant TEC, and binning each barchart in mean intra-TIPP lag on the abscissa. The group of TIPPs with the lowest TEC is shown in the upper-left barchart, while the group with the highest TEC is shown in the lower-right barchart. We make three observations:
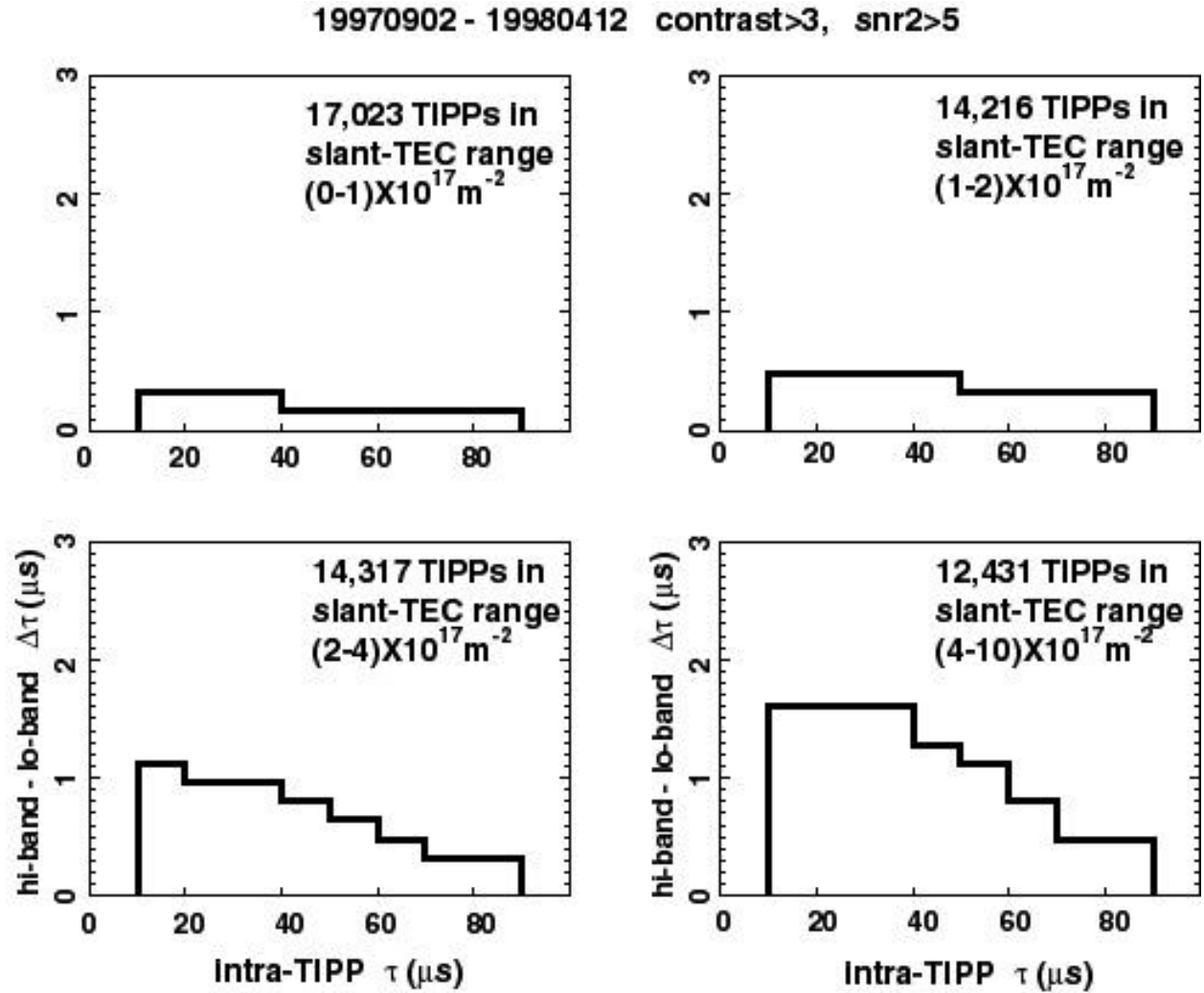
Figure 18: Similar to Figure 17, but with intra-TIPP separation as the abscissa, and each barchart corresponding to a different subrange of inferred slant-TEC.

(1) The median defect in *all* mean-lag bins, and in all TEC groups, is positive. This is consistent with the GR hypothesis and inconsistent with the HAD hypothesis.

(2) The defect is greatest for the highest-TEC group, and smallest for the lowest-TEC group.

(3) Within each barchart, the defect decreases for increasing mean intra-TIPP lag. This is consistent with the GR hypothesis and inconsistent with the HAD hypothesis.

We conclude that the TIPP data of FORTÉ's first seven months are consistent with a ground-reflection rather than a high-altitude-discharge origin of the second pulse.

6. VHF frequency spectrum of TIPP power: Bimodal distribution?

As noted in Sections 1 and 2 above, the Blackbeard trigger was based on the total instantaneous power within a broad band (up to 75 MHz) and hence required a brighter VHF lightning event for the trigger to compete with man-made radio noise. Blackbeard observations of TIPPs [*Holden et al.*, 1995; *Massey and Holden*, 1995; *Massey et al.*, 1998] were also consistent with the idea that the TIPP spectrum might be approximately flat from 25 - 200 MHz, i.e. over much of the VHF. This spectral flatness, plus the TIPPs' overall brightness compared to common VHF emissions from lightning [*Massey et al.*, 1998], were consistent with TIPPs' being related to a very bright VHF pulses seen elsewhere at ground level [*Le Vine*, 1980] and associated with unusual electric-field waveforms called "narrow positive bipolar pulses" or NPBPs [*Willet et al.*, 1989]. More recently a study [*Smith et al.*, 1998] of airmass storms in the New Mexico region has shown that NPBPs (and hence, implicitly, the intense rf emissions associated with NPBPs) are radiated from an event high in the most powerful convection cores and region of highest radar reflectivity. This study [*Smith et al.*, 1998] also showed that the NPBPs are temporally isolated compared to more common field-change signatures, an observation which had been made earlier with respect to the intense rf emissions.

The FORTÉ trigger scheme allows relatively clean recording of many lightning VHF signatures, not just the unusual VHF events which seem to be associated with NPBPs. The FORTÉ trigger can be derived from either the lo-band or the hi-band 22-MHz-wide channels, and this choice apparently introduces a significant bias in the nature of lightning VHF signatures which we collect. The simultaneous recording of two channels, one centered at about 38 MHz, and the other at about 130 MHz, allows us to routinely characterize the VHF spectrum of the event by the ratio of the hi-band to the lo-band peak powers (reckoned after carrier-suppression and optimal dechirping).

This peak-power ratio would have been on the order of unity for the intense, white-spectrum events seen by Blackbeard and seen earlier from the ground [*Le Vine*, 1980; *Willet et al.*, 1989]. For conventional lightning emissions, on the other hand, the power ratio of 130 MHz to 38 MHz might be expected to be on the order of 0.1 or less [*Willet et al.*, 1989]. Figure 19 shows a histogram (on a log-log scale, so that the right end has more bins than the left) of the peak-power ratio of FORTÉ lightning events (*not* just TIPPs), using a histogram binsize of 0.01. The top panel is for all 429,230 events with contrast >3 having the 38-MHz and 130-MHz center-frequency combination. The second panel is for the subset of these events having a lo-band trigger, and the lowermost panel is for the subset with a hi-band trigger.

From Figure 19 we can state:

(1) The probability *density* of low values of the peak-power ratio is greater than of high values of that ratio. That is, for a given binsize, steeply-rolling-off-spectrum events are more probable than are white-spectrum events.

(2) This trend is more obvious with the pure lo-band trigger subgroup (middle panel).

(3) The use of a hi-band trigger, performed in only 6% of the recorded events, results in a bimodal distribution in the peak-power ratio and hence in the spectral slope.

The peak-power ratio P_H/P_L is now used to explore the behavior of TIPPs, as opposed to all events shown in Figure 19. First, we find that the TIPP peak-power histograms are indistinguishable from Figure 19, except that there are fewer events overall. We find however that there is a profound difference in how isolated TIPPs are from neighboring TIPPs, depending on their peak-power ratio. We use as a metric of isolatedness of a lightning event the time separation between that event and its nearest neighbor of the same class, say of a TIPP from the neighboring TIPP. Figure 20 shows a histogram of the nearest-neighbor separation for 71,437 TIPPs with
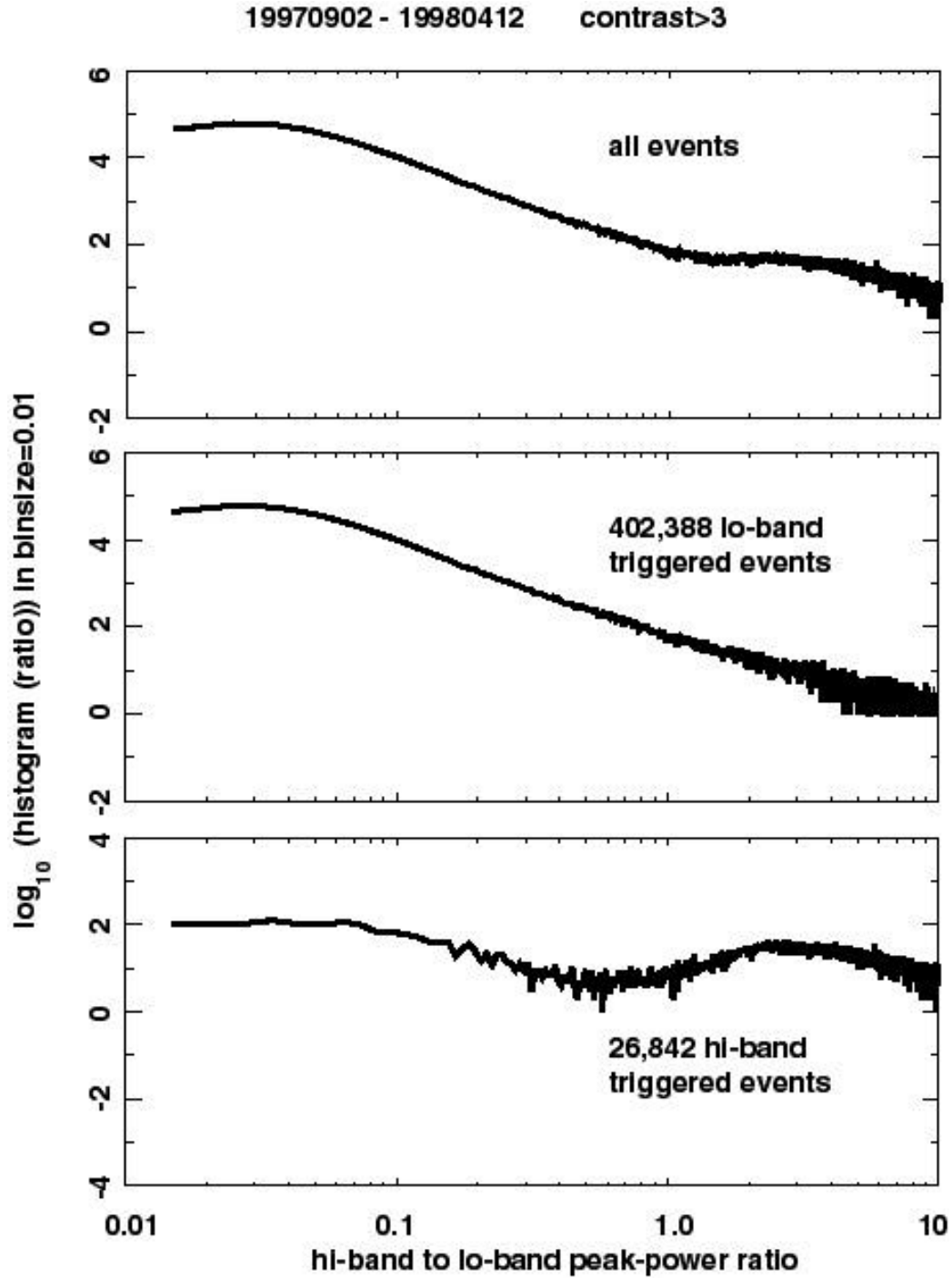
Figure 19: Histograms of the hi-band to lo-band peak-power ratio (after prewhitening and optimal dechirping) for all events with contrast >3 (top panel), only the lo-band triggered events with contrast >3 (middle panel), and only the hi-band triggered events with contrast >3 (bottom panel). Both scales are logarithmic, though the histogram is linear (binsize = 0.01) in the abscissa. Thus there are more bins on the right than on the left.
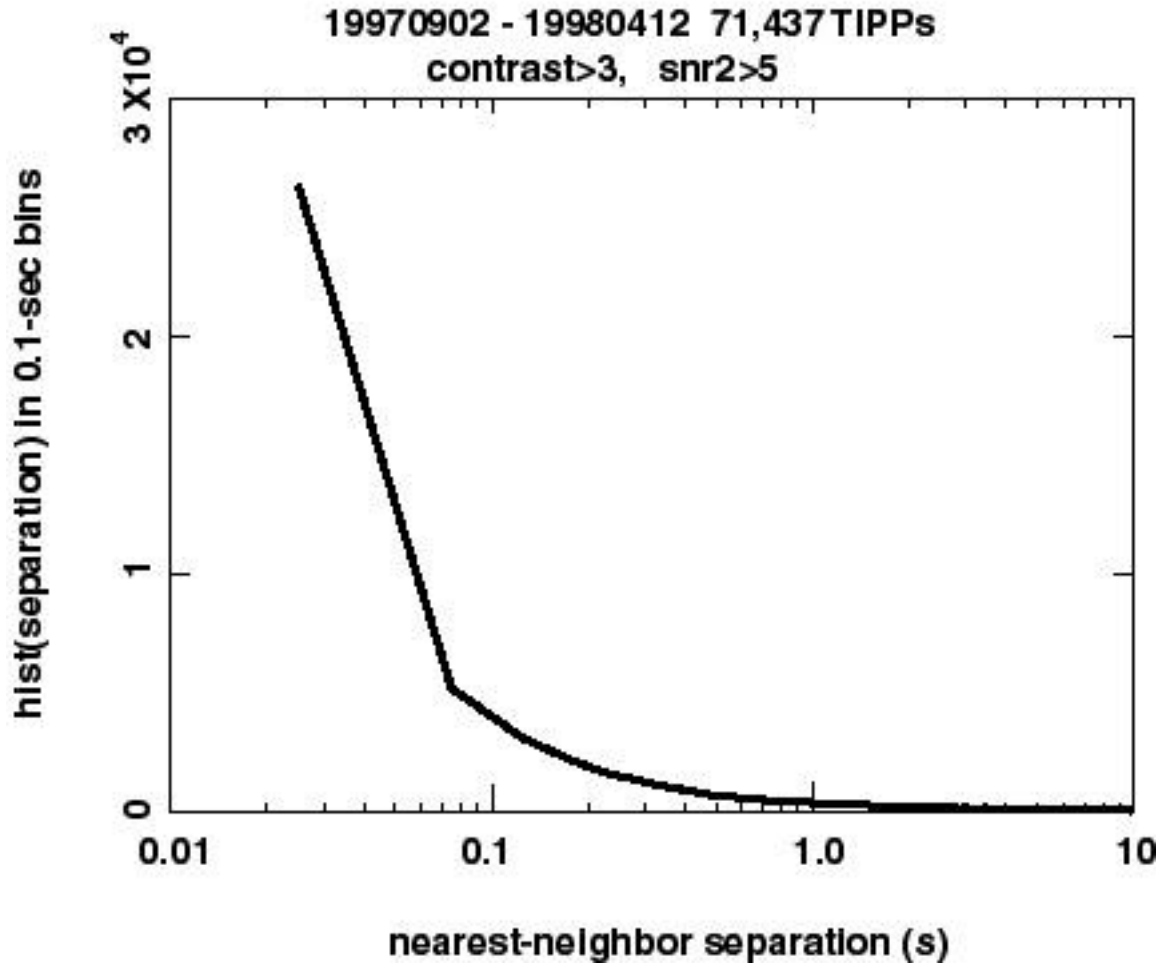
Figure 20: Histogram of nearest-neighbor separation for TIPPs with contrast >3 and snr2 > 5. The abscissa is logarithmic, though the histogram is linear (binsize = 0.1 s) in the abscissa. Thus there are more bins on the right than on the left.

contrast>3 and snr2>5 and having the 38-MHz and 130-MHz center-frequency combination. The plot is linear ordinate versus logarithmic abscissa, with constant abscissa bin of 0.1 s. Evidently the probability *density* of closely-neighboring TIPPs is much greater than of widely-separated TIPPs.

Figure 21 shows a similar histogram for two classes of TIPPs separately. The majority class (66,622 TIPPs) has a peak-power ratio <0.3, while the minority class (4,815 TIPPs) has a peak-power ratio >0.3. It is seen that the high-ratio (>0.3) TIPPs are much

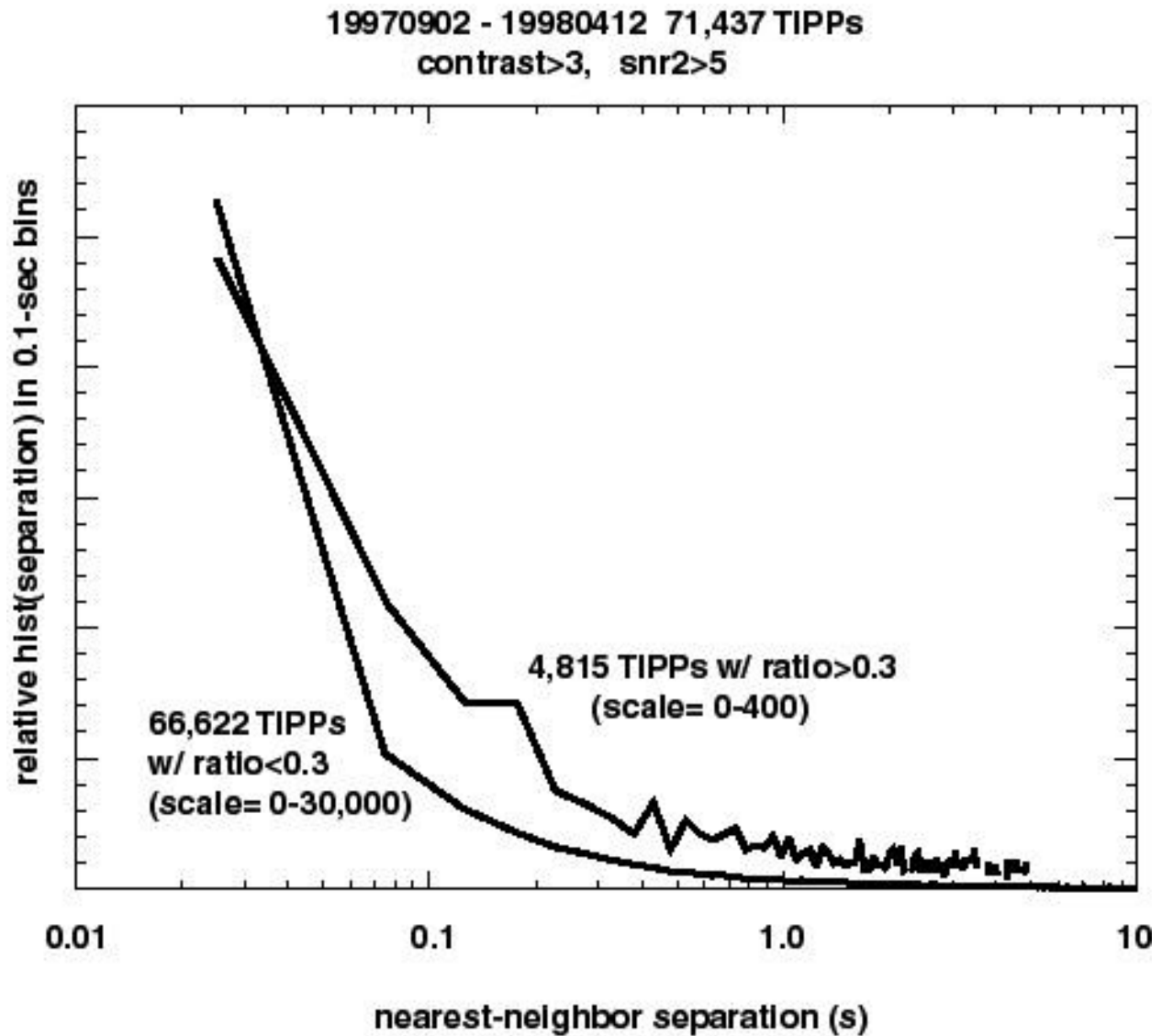## 19970902 - 19980412 71,437 TIPPs
contrast>3, snr2>5

Figure 21: Similar to Figure 20, but done separately for flat-spectrum events (top curve) and steep-spectrum events (lower curve). The ordinate scale for each is noted. Evidently the flat-spectrum events are more likely to have large nearest-neighbor separations than are the steep-spectrum events.

more likely to be isolated (say, nearest-neighbor separations >0.1 s) than are the low-ratio (<0.3) TIPPs. The difference is not subtle. This bimodal distribution of the peak-power-ratio distribution, and the grossly different isolatedness of TIPPs of either mode, reinforce our suspicion that the high-ratio (>0.3) TIPPs (and only the high-ratio TIPPs) we see with FORTÉ are associated with the same phenomenon seen by Blackbeard

as "TIPPs" and seen on the ground as NPBP-related VHF pulses [*Le Vine*, 1980; *Smith et al.*, 1998; *Willet et al.*, 1989].

7. Outlook for height analysis of FORTÉ lightning VHF signatures

Given the essential confirmation that TIPPs FORTÉ observes are double pulses *because of a ground reflection*, we can look forward to performing height analysis on storm VHF impulsive emission centers. By using other information (e.g., geolocation of flashes by very low frequency sferic receiver arrays) to determine the latitude and longitude of the VHF emitter responsible for a FORTÉ event, we can then infer the altitude of the emitter, from the intra-TIPP pulse lag (see Eq. 10.) In fact, some start has been made in this direction using Blackbeard [*Zuelsdorf et al.*, 1997].

In particular, the ability of FORTÉ to mosaic-together short (say, 400-μs) events allows us to record the migration of breakdown processes during intra-flash sequences, thus performing in one dimension (vertical) what a time-of-arrival system [*Oetzel and Pierce*, 1969] performs in three dimensions, or an interferometric system [*Rhodes et al.*, 1994; *Shao et al.*, 1996] performs in two dimensions.

Figure 22 shows the intra-TIPP lag (upper panel) and inferred slant TEC (lower panel) during a single flash lasting less than 0.5 s. Starting at 0.19 s into the time-series, there is a rise in the height of the emission center, while a lower center remains sporadically active during the remainder of the flash. We do not have independent geolocation of this flash (occuring in the South Pacific), so the interpetation of the intra-TIPP lag in terms of height above Earth is subject to an unknown (but constant) scaling factor. If we assume that the storm is at nadir, then the top-emitter level asymptotes to a height of 12 km (corresponding to 80-μs lag), while the sporadic lower level remains steady at 5 km (corresponding to 35-μs lag). By comparison, had the storm not been at nadir, but rather 600 km off to the side, then the maximum satellite elevation angle would
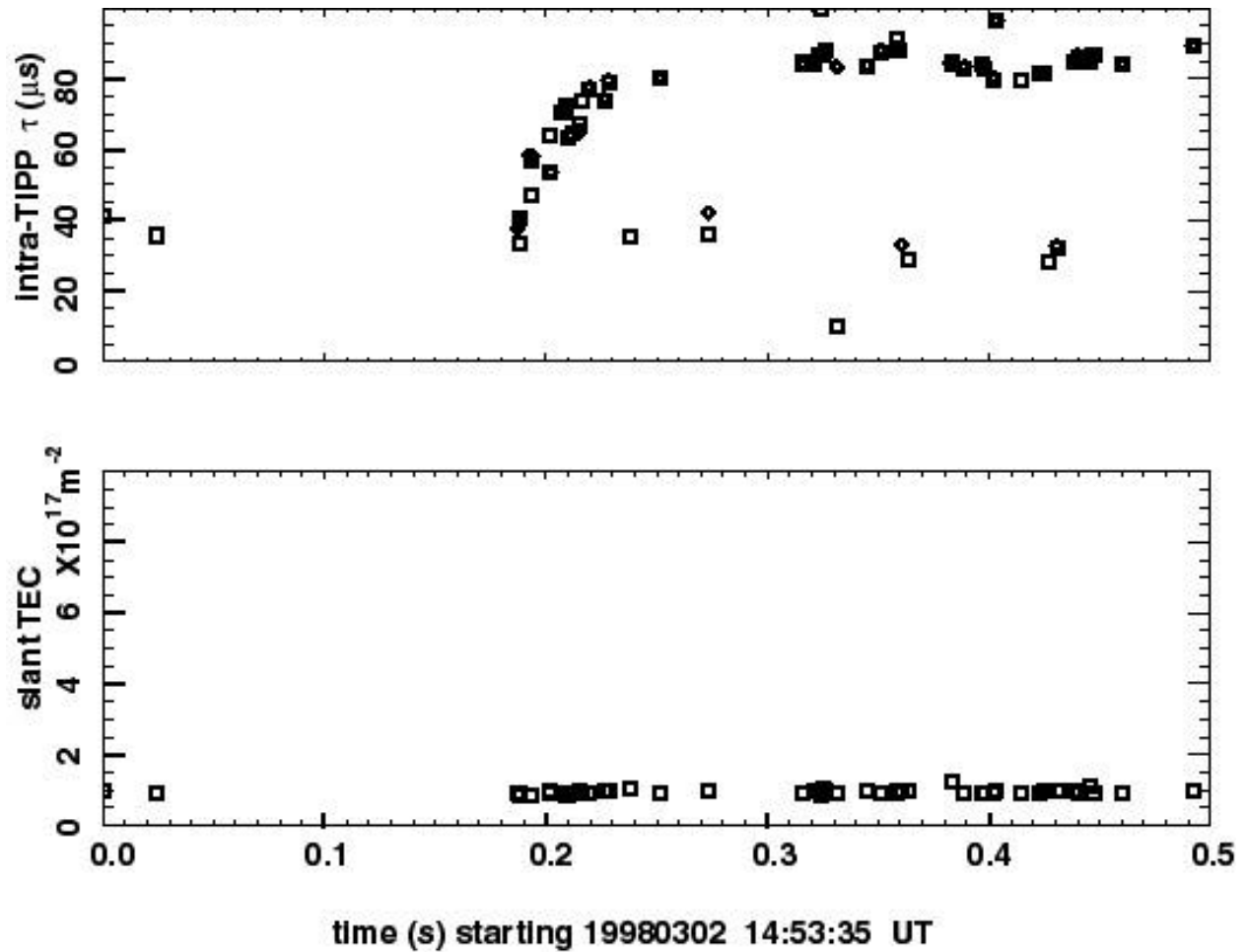
Figure 22: Intra-TIPP separation (top panel) and lo-band-inferred slant TEC (bottom panel) versus time for a single flash. In the top panel, the squares are for lo-band, and the diamonds are for hi-band. Note that the total abscissa range

have been 48°, and inferred emission heights would have been 70% of those from a nadir location. A forthcoming publication will describe in detail the application of FORTÉ TIPP height analysis to emissions from storms which have been geolocated by time-coincidence with other data sources, so that the height can be unambiguously inferred.

The constancy of the TEC data in Figure 22 (lower panel) is an indicator that the events occur for constant nadir angle (from the satellite). Given the clustering of these events within a given apparent flash, we interpret the constancy of TEC to be a confirmation of the common spatial origin of these events. This is typical of the behavior of flash-clustered VHF events seen by FORTÉ: Events occuring within, say, 0.3 second of each other are overwhelmingly likely to have effectively identical TEC.

This is consistent with the FORTÉ viewed area's producing flashes which typically do not overlap in time.

8. Conclusions

VHF lightning observations by FORTÉ are providing new capability to monitor lightning activity. The full benefits of FORTÉ's flexible VHF programming and large VHF-data memory will become even more important when its data are combined with data from ground-based sferic arrays, VHF interferometers, VHF time-of-arrival systems, radars, satellite remote-sensing imagery, and FORTÉ's own optical imager. The purpose of this paper has been to survey the range of FORTÉ's VHF capabilities and initial results.

The most dramatic new result is a very compelling confirmation that the second pulse in TIPPs comes from ground reflections, not from a high-altitude discharge.

Another key new finding is that TIPPs in recurrent-emission storms provide both intra-TIPP lag and slant-TEC curves (as a function of satellite position) curves which may provide the basis for autonomous geolocation of the emitter.

References

Enemark, D.C., and M.E. Shipley, The FORTE receiver and sub-band triggering unit, in *Eighth Annual American Institute of Aeronautics and Astronautics (AIAA)/ Utah State University (USU) Conference on Small Satellites*, Utah State University, Logan, Utah, 1994.

Holden, D.N., C.P. Munson, and J.C. Devenport, Satellite observations of transionospheric pulse pairs, *Geophys. Res. Lett.*, *22* (8), 889-892, 1995.

Le Vine, D.M., Sources of the strongest rf radiation from lightning, *J. Geophys. Res.*, *85* (C7), 4091-4095, 1980.

Massey, R.S., and D.N. Holden, Phenomenology of transionospheric pulse pairs, *Radio Sci.*, *30* (5), 1645-1659, 1995.

Massey, R.S., D.N. Holden, and X.-M. Shao, Phenomenology of trans-ionospheric pulse pairs, *Radio Science*, *submitted*, 1998.

Oetzel, G.N., and E.T. Pierce, VHF technique for locating lightning, *Radio Sci.*, *4* (3), 199-202, 1969.

Rhodes, C.T., X.M. Shao, P.R. Krehbiel, R.J. Thomas, and C.O. Hayenga, Observations of lightning phenomena using radio interferometry, *J. Geophys. Res.*, *99*, 13059-13082, 1994.

Roussel-Dupré, R., and A.V. Gurevich, On runaway breakdown and upward propagating discharges, *J. Geophys. Res.*, *101* (A2), 2297-2311, 1996.

Shao, X.M., D.N. Holden, and C.T. Rhodes, Broad band radio interferometry for lightning observations, *Geophys. Res. Lett.*, *23* (15), 1917-1920, 1996.

Smith, D.A., X.M. Shao, D.N. Holden, C.T. Rhodes, M. Brook, P.R. Krehbiel, M. Stanley, W. Rison, and R.J. Thomas, Distinct, isolated thunderstorm radio emissions, *J. Geophys. Res.*, *submitted*, 1998.

Willet, J.C., J.C. Bailey, and E.P. Krider, A class of unusual lightning electric field waveforms with very strong high-frequency radiation, *J. Geophys. Res.*, *94* (D13), 16255-16267, 1989.

Zuelsdorf, R.S., C. Casler, R.J. Strangeway, C.T. Russell, and R.C. Franz, Ground detection of trans-ionospheric pulsed pairs by stations in the National Lightning Detection Network, *Geophys. Res. Lett.*, *25* (4), 481-484, 1998.

Zuelsdorf, R.S., R.J. Strangeway, C.T. Russell, C. Casler, H.J. Christian, and R.C. Franz, Transionospheric pulse pairs (TIPPs): Their geographic distributions and seasonal variations, *Geophys. Res. Lett.*, *24* (24), 3165-3168, 1997.

[1]Corresponding author: Mail Stop D466, LANL, Los Alamos, NM 87544

e-mail: ajacobson@lanl.gov   (505) 667-9656